

RESEARCH ARTICLE

10.1002/2013JD020566

Special Section:

The Geoengineering Model Intercomparison Project (GeoMIP)

Key Points:

- Different processes affect ozone in stratospheric sulfate aerosol geoengineering
- Suppression of NO_x cycle becomes more important than ClO_x depleting cycle
- Polar UV-B increases by 5% annually and 12% in spring

Correspondence to:

G. Pitari,
gianni.pitari@aquila.infn.it

Citation:

Pitari, G., V. Aquila, B. Kravitz, A. Robock, S. Watanabe, I. Cionni, N. De Luca, G. Di Genova, E. Mancini, and S. Tilmes (2014), Stratospheric ozone response to sulfate geoengineering: Results from the Geoengineering Model Intercomparison Project (GeoMIP), *J. Geophys. Res. Atmos.*, 119, 2629–2653, doi:10.1002/2013JD020566.

Received 22 JUL 2013

Accepted 31 JAN 2014

Accepted article online 5 FEB 2014

Published online 5 MAR 2014

Stratospheric ozone response to sulfate geoengineering: Results from the Geoengineering Model Intercomparison Project (GeoMIP)

Giovanni Pitari^{1,2}, Valentina Aquila³, Ben Kravitz⁴, Alan Robock⁵, Shingo Watanabe⁶, Irene Cionni⁷, Natalia De Luca¹, Glauco Di Genova¹, Eva Mancini¹, and Simone Tilmes⁸

¹Department of Physical and Chemical Sciences, Università degli Studi de L'Aquila, L'Aquila, Italy, ²Center of Excellence CETEMPS, Università degli Studi de L'Aquila, L'Aquila, Italy, ³GESTAR/Johns Hopkins University, NASA GSFC, Greenbelt, Maryland, USA, ⁴Atmospheric Sciences and Global Change Division, Pacific Northwest National Laboratory, Richland, Washington, USA, ⁵Department of Environmental Sciences, Rutgers University, New Brunswick, New Jersey, USA, ⁶Japan Agency for Marine–Earth Science and Technology, Yokohama, Japan, ⁷ENEA, Ente per le Nuove Tecnologie, l'Energia e l'Ambiente, Rome, Italy, ⁸National Center for Atmospheric Research, Boulder, Colorado, USA

Abstract Geoengineering with stratospheric sulfate aerosols has been proposed as a means of temporarily cooling the planet, alleviating some of the side effects of anthropogenic CO₂ emissions. However, one of the known side effects of stratospheric injections of sulfate aerosols under present-day conditions is a general decrease in ozone concentrations. Here we present the results from two general circulation models and two coupled chemistry–climate models within the experiments G3 and G4 of the Geoengineering Model Intercomparison Project. On average, the models simulate in G4 an increase in sulfate aerosol surface area density similar to conditions a year after the Mount Pinatubo eruption and a decrease in globally averaged ozone by 1.1–2.1 DU (Dobson unit, 1 DU = 0.001 atm cm) during the central decade of the experiment (2040–2049). Enhanced heterogeneous chemistry on sulfate aerosols leads to an ozone increase in low and middle latitudes, whereas enhanced heterogeneous reactions in polar regions and increased tropical upwelling lead to a reduction of stratospheric ozone. The increase in UV-B radiation at the surface due to ozone depletion is offset by the screening due to the aerosols in the tropics and midlatitudes, while in polar regions the UV-B radiation is increased by 5% on average, with 12% peak increases during springtime. The contribution of ozone changes to the tropopause radiative forcing during 2040–2049 is found to be less than -0.1 W m^{-2} . After 2050, because of decreasing ClO_x concentrations, the suppression of the NO_x cycle becomes more important than destruction of ozone by ClO_x, causing an increase in total stratospheric ozone.

1. Introduction

Geoengineering has been proposed as a means of deliberately, temporarily altering the climate to alleviate some of the consequences of anthropogenic greenhouse gas emissions [e.g., Shepherd *et al.*, 2009]. One proposed method involves mimicking a volcanic eruption by injecting sulfate aerosol precursors (e.g., SO₂) into the stratosphere [Budyko, 1974; Crutzen, 2006]. Large volcanic eruptions are capable of injecting considerable amounts of particles and sulfur gases above the tropopause, potentially increasing the stratospheric aerosol optical depth by 1 order of magnitude or more. Nucleation of H₂SO₄ vapor derived from the initial volcanic SO₂ plume [Bluth *et al.*, 1992; Read *et al.*, 1993] can produce an optically thick cloud of sulfate aerosols [McCormick and Veiga, 1992; Lambert *et al.*, 1993; Long and Stowe, 1994], which are highly reflective in the visible and UV, causing a substantial decrease in radiation reaching the Earth surface and, subsequently, a general surface cooling. The 1991 eruption of Pinatubo, for instance, resulted in reductions in globally averaged surface air temperature by approximately 0.5°C [Soden *et al.*, 2002], with a calculated globally averaged net radiative flux change at the tropopause that reached its maximum during January 1992 (-4.5 W/m^2 , with $\tau = 0.15$) [Hansen *et al.*, 1992], decreasing afterward with an *e*-folding time of about 1 year (-1.2 W/m^2 during June 1993). At the same time, however, the volcanic aerosol has other atmospheric effects, such as changes in atmospheric dynamics and ozone concentrations. Measurements taken a few months after the Pinatubo eruption revealed a 2–3 K warming in the tropical lower stratosphere [Labitzke and McCormick, 1992; Young *et al.*, 1994] and a decrease of about 20 DU (Dobson unit, 1 DU = 0.001 atm cm) of the tropical ozone column in the 16–28 km layer during October–November 1991 [Grant *et al.*, 1992; Schoeberl

et al., 1993]. A model study by *Telford et al.* [2009] calculated a global ozone column decrease by about 7 DU because of the Mount Pinatubo eruption.

A perturbation of the stratospheric aerosol may affect the stratospheric ozone concentrations mainly via changes in the following: (a) photolysis rates (O_2 in particular); (b) heterogeneous chemistry on the surface of sulfuric acid aerosols; (c) homogenous chemistry due to temperature changes; (d) heterogeneous chemistry on the surface of polar stratospheric clouds (PSC), which are enhanced because of temperature changes and increasing population of sulfate aerosols condensation nuclei; and (e) perturbations of the stratospheric large-scale circulation. Photochemical processes (a)–(c) are mostly relevant for the tropics and midlatitudes, whereas effect (d) could be important for polar ozone depletion. Changes in heterogeneous chemistry (b) lead to an enhancement of the ozone-depleting HO_x and ClO_x cycles and a suppression of the ozone-depleting NO_x cycle. This generally results in a decrease of ozone in the lower stratosphere and an increase above [*Tie and Brasseur*, 1995].

Although the stratospheric effects due to volcanic eruptions are well studied, the expected effects due to geoengineering have received less attention. *Tilmes et al.* [2008] reported that geoengineering with sulfate aerosols could enhance stratospheric ozone destruction and delay the recovery of the Antarctic ozone hole by 30–70 years. Further, the acceleration of ozone loss cycles over the polar regions due to the increase of aerosols may significantly decrease the ozone column and increase erythemal UV by up to 5% in middle and high latitudes and 10% over Antarctica, by midcentury halogen conditions [*Tilmes et al.*, 2012].

Perturbations of transport of stratospheric tracer species may result from dynamical changes due to local stratospheric heating and cooling of the surface due to the scattering of incoming solar radiation by the volcanic (or geoengineering) particles [*Hansen et al.*, 1992; *Lacis et al.*, 1992; *Stenchikov et al.*, 1998; *Kirchner et al.*, 1999]. The stratospheric mean meridional circulation is affected by local aerosol radiative heating (mostly located in the tropical lower stratosphere). At the same time, the planetary wave propagation in the middle- to high-latitude lower stratosphere is altered as a consequence of changing atmospheric stability due to the surface cooling. The stratospheric diabatic heating perturbation is introduced by the following: (a) direct aerosol interaction with solar and planetary radiation and indirect ozone absorption of the aerosol diffused solar radiation [*Pitari*, 1993; *McCormick et al.*, 1995]; and (b) changing ozone absorption of incoming solar and outgoing planetary radiation, as a consequence of ozone losses produced by heterogeneous chemistry on volcanic aerosols, perturbed photolysis rates, and stratospheric large scale transport [*Prather*, 1992; *Kinne et al.*, 1992; *Schoeberl et al.*, 1993].

The Geoengineering Model Intercomparison Project (GeoMIP) aims to determine the robust features of climate model response to four core geoengineering experiments involving uniform solar irradiance reduction and stratospheric injections of sulfate aerosol precursors [*Kravitz et al.*, 2011a]. In this study, we investigate the stratospheric ozone response in experiments G3 and G4, with focus on photochemical perturbations. Experiments G1 and G2, on the other hand, are not covered here because they solely consider reductions in solar irradiance, rather than stratospheric sulfate aerosol injection [*Kravitz et al.*, 2011a]. Both experiments G3 and G4 have a background anthropogenic forcing profile corresponding to Representative Concentration Pathway 4.5 (RCP4.5) [*Taylor et al.*, 2012]. Beginning in 2020, G3 involves transient stratospheric injections of SO_2 to maintain top-of-atmosphere net radiation at 2020 levels. G4, on the other hand, involves a constant continuous stratospheric injection rate of 5 Tg SO_2 per year. These simulations are performed for 50 years, after which geoengineering is immediately ceased; the simulations are then run for an additional 20 years to determine the climate response of the termination effect [e.g., *Jones et al.*, 2013].

The paper is organized into four subsequent sections. Section 2 includes a description of participating models. Section 3 discusses models results regarding stratospheric aerosols (background and GeoMIP perturbations). Section 4 analyzes changes in stratospheric ozone in terms of aerosol-induced perturbations in chemical production and loss, vertical profiles, and total column, as well as an evaluation of past ozone distribution and trends. In the same section we also present the changes in tropopause radiative forcing and surface UV. The main conclusions are summarized in section 5.

2. Description of Models

Participating models in this study are as follows: ULAQ-CCM (University of L'Aquila Chemistry Climate Model), GISS-E2-R (Goddard Institute for Space Science Model E2), MIROC-ESM-CHEM (Model for Interdisciplinary

Table 1. Summary of Model Runs (nhc=No Heterogeneous Chemistry on Sulfate Aerosols)

	RCP4.5	G3	G4
ULAQ-CCM	2	2 (+2 nhc)	2 (+2 nhc)
GISS-E2-R	3	3 nhc	3 nhc
MIROC-ESM-CHEM	1		4
GEOSCCM	2		2

Research on Climate), and GEOSCCM (Goddard Earth Observing System Chemistry Climate Model). A summary of the performed model runs is presented in Table 1.

Table 2 summarizes the major differences among the participating models, in terms of horizontal and vertical resolution, ocean

coupling, quasi-biennial oscillation (QBO) parameterization, treatment of stratospheric aerosol, and aerosol-chemistry coupling. Two of the models (GISS-E2-R and MIROC-ESM-CHEM) are fully coupled Earth-system models, while ULAQ-CCM and GEOSCCM are forced with sea surface temperatures (SST) and sea ice concentrations from RCP4.5 future simulations performed with the Community Earth System Model (CESM) [Gent et al., 2011]. MIROC-ESM-CHEM and GEOSCCM simulate the QBO internally, using a gravity wave drag (GWD) parameterization. Hence, in these two models, the QBO might be modified by the radiative interaction of the aerosol. ULAQ-CCM, on the other hand, uses a nudged QBO; GISS-E2-R does not include a QBO simulation, and the equatorial stratosphere is in a condition of perpetual easterlies.

ULAQ-CCM, GISS-E2-R, and GEOSCCM simulate the formation of sulfate aerosol starting from the oxidation of SO₂, while MIROC-ESM-CHEM uses a prescribed stratospheric aerosol optical depth (AOD) as a function of latitude, height, and month. Only ULAQ-CCM includes a module for aerosol microphysics for the explicit prediction of the aerosol size distribution; the other models prescribe fixed aerosol size distributions for radiative calculations (in MIROC-ESM-CHEM, GEOSCCM, and GISS-E2-R) and aerosol sedimentation rates (in GEOSCCM and GISS-E2-R). Aerosol heating rates in solar near-infrared (NIR) and planetary longwave radiation are included in all models. Ozone photochemistry with sensitivity of photolysis to aerosol scattering is included in ULAQ-CCM, GISS-E2-R, and MIROC-ESM-CHEM; a lookup table for photo-dissociation rates is used in GEOSCCM. Heterogeneous chemical reactions on the surface of sulfate aerosols, with feedback on NO_x chemistry, are included in ULAQ-CCM, MIROC-ESM-CHEM, and GEOSCCM. They are not included in GISS-E2-R and in specific sensitivity runs of ULAQ-CCM. The acronym “nhc” used throughout the paper stands for “no heterogeneous chemistry on stratospheric sulfate aerosol.” More details on each model are included in the following sections.

2.1. ULAQ-CCM

The University of L'Aquila model is a global scale climate-chemistry coupled model (ULAQ-CCM) extending from the surface to the mesosphere (0.04 hPa); model features are described in Pitari et al. [2002], Eyring et al. [2006], and Morgenstern et al. [2010]. Following the participation in the second phase of the Chemistry-Climate Model Validation Activity (CCMVal-2) [Morgenstern et al., 2010], some important updates have been made to the model: increase of horizontal and vertical resolution, now T21 with 126 log pressure levels

Table 2. Summary of Main Model Features^a

Model	Resolution ^b	Ocean	QBO	Stratospheric Aerosol			Aerosol Effect on Chemistry		
				Source	r_{eff} (μm) G4	r_{eff} (μm) RCP4.5	Heterogeneous Chemistry on Aerosol	Heterogeneous Chemistry on PSCs	Aerosol Impact on Photolysis
ULAQ-CCM	5° × 6°, L126 Top: 0.04 hPa	Prescribed SSTs	Nudged	From SO ₂	0.61 ^c	0.19 ^c	Yes	Yes	Yes
GISS-E2-R	2° × 2.5°, L40 Top: 0.1 hPa	Coupled	Not included	From SO ₂	0.35	0.15	No	Yes	Yes
MIROC-ESM-CHEM	2° × 2.5°, L80 Top: 0.01 hPa	Coupled	Internal ^d	Prescribed AOD	0.24	0.24	Yes	Yes	Yes
GEOSCCM	2° × 2.5°, L72 Top: 0.01 hPa	Prescribed SSTs	Internal ^d	From SO ₂	0.60	0.20 ^e	Yes	Yes	No

^aColumns 6–7 show the stratospheric aerosol effective radius (μm) at 20 km over the tropics (2040–2049). Values deduced from SAGE-II observations are: 0.22 ± 0.02 μm as an average over 1999–2000 for unperturbed background conditions and 0.57 ± 0.03 μm as an average over July 1992–June 1993 for a volcanic perturbation (i.e., Pinatubo) comparable in magnitude to G4 (in terms of average stratospheric mass burden of sulfate; see text).

^bLatitude by longitude horizontal resolution, number of vertical layers, and model top atmospheric pressure.

^cIncludes aerosol microphysics.

^dQBO internally generated using a gravity wave drag parameterization and resolved wave forcing.

^eGEOSCCM is forced with background aerosol area surface density from SAGE data for 1999.

(approximate pressure altitude increment of 568 m); inclusion of a parameterization for the formation of upper tropospheric cirrus cloud ice particles [Kärcher and Lohmann, 2002]; update of species cross sections using recommendations by Sander *et al.* [2011] and Schumann-Runge bands treatment following the parameterization of Minschwaner *et al.* [1993] based on fixed-temperature opacity distribution function formulation; and upgrade of the radiative transfer code for calculations of photolysis, solar heating rates, and top-of-atmosphere radiative forcing. The oceanic surface temperature is prescribed from the Hadley Centre for Climatic Prediction and Research [Rayner *et al.*, 2003]. ULAQ-CCM includes a nudged QBO, by extrapolating in future the historical time series of monthly means from Singapore data and a representation of the solar cycle, by extrapolating in future the historical time series of monthly data of top-of-atmosphere spectral solar fluxes from the last observed solar cycle [Lean, 2000]. The chemistry module is organized with all medium and short-lived species grouped in the families O_x , NO_y , NO_x , CHO_x , Cl_y , Br_y , SO_x , and also includes aerosols. In total, there are 40 transported species, 26 species at photochemical equilibrium and 57 size categories for aerosols. The model includes the major components of stratospheric and tropospheric aerosols (sulfate, carbonaceous, soil dust, sea salt, and PSCs). The size distributions of sulfate (both tropospheric and stratospheric) and PSC particles are calculated using an interactive and mass conserving microphysical code for aerosol formation and growth, including a gas particle conversion scheme. New sulfuric acid particles are formed via homogeneous nucleation, followed by coagulation and condensation growth; stratospheric aerosols are lost via evaporation in the upper stratosphere and downward transport and sedimentation into the troposphere. For the GeoMIP simulations, SO_2 was injected throughout the altitude range of 18–24 km at 0° longitude on the equator. Lower stratospheric denitrification and dehydration are calculated using the predicted size distribution of PSC particles. Heterogeneous reactions on sulfate and PSC aerosols are included in the chemistry module [Pitari *et al.*, 2002], with the hydrolysis of N_2O_5 and $BrONO_2$ being the two most important reactions on the surface of stratospheric sulfuric acid aerosols at midlatitudes. The updated radiative transfer module, operating online in the ULAQ-CCM, is a two-stream delta-Eddington approximation model [Toon *et al.*, 1989], used for chemical species photolysis rate calculation in ultraviolet (UV)-visible (VIS) wavelengths and for solar heating rates and radiative forcing in UV-VIS-near-infrared (NIR) bands. Top-of-atmosphere solar fluxes are taken from SUSIM-SL2 and LOWTRAN7 and are integrated on the wavelength bins used in the model, of which there are 150 in the UV and visible range and 100 in the NIR range, covering the solar spectrum from Lyman- α up to $7 \mu\text{m}$. Sun-Earth distance is calculated daily as a function of orbit eccentricity, and the solar cycle is included. Sphericity is treated by means of Chapman functions [Dahlback and Stamnes, 1991]. Refraction is taken into account with an iterated ray-tracing technique in a simple exponential refraction model. Optical depths take into account Rayleigh scattering, radiation absorption from O_3 , O_2 , NO_2 , SO_2 , H_2O , CO_2 , and scattering/absorption from aerosol particles. Planetary radiation heating rates and top-of-atmosphere/tropopause forcings are calculated including absorption/emission by CO_2 (15 μm band), O_3 (9.6 μm band), H_2O , and aerosols, using well-tested absorptivity formulas through a correlated-k method. Aerosol extinction values are passed daily from the ULAQ-CCM aerosol module to the radiative transfer module, with appropriate wavelength-dependent values of extinction coefficient, asymmetry factor, and single scattering albedo, given the calculated size distribution of the particles. Surface albedo is taken from MERRA 2-D hourly averaged data [Rienecker *et al.*, 2011]. The ULAQ model calculations of photolysis rates and surface and top-of-atmosphere radiative fluxes have been validated in the framework of the CCMVal and AEROCOM intercomparison projects [Chipperfield *et al.*, 2013; Randles *et al.*, 2013].

2.2. GISS-E2-R

GISS-E2-R is a fully coupled atmosphere-ocean general circulation model, developed by the National Aeronautics and Space Administration's Goddard Institute for Space Studies (GISS), which is a contributor to the Coupled Model Intercomparison Project Phase 5 (CMIP5) [Schmidt *et al.*, 2006; Taylor *et al.*, 2012]. The atmospheric model has a horizontal resolution of 2° latitude by 2.5° longitude and 40 vertical layers extending through the mesosphere (model top of 0.1 hPa). It is coupled to the Russell ocean model [Russell *et al.*, 1995] which has horizontal resolution of 1° latitude by 1.25° longitude and 32 vertical layers. The version discussed here includes full stratospheric gas phase chemistry [Shindell *et al.*, 2006]; heterogeneous reactions on the surface of the sulfate aerosols are not included. However, GISS-E2-R does have a representation of heterogeneous chemistry facilitated by polar stratospheric clouds. Photolysis in the stratosphere is included and varies dynamically as a function of temperature, pressure, solar output, cloudiness, albedo, and ozone concentration. Ozone and methane are computed at the model's resolution and are radiatively interactive

with model tracers, i.e., they modify heating rates and are chemically active. Formation of sulfate aerosols is specified by a reaction rate in which an aerosol dry radius is specified, as described by Koch *et al.* [2006]. The aerosols then grow hygroscopically according to ambient relative humidity per the formulas of Tang [1996]. In this study, the aerosol dry radius is specified to be 0.35 μm , which is the same specification as was used by Robock *et al.* [2008] in their simulations of the 1991 eruption of Mount Pinatubo and results in an approximately Pinatubo-sized aerosol in simulations of volcanic eruptions, per GeoMIP specifications [Kravitz *et al.*, 2011b]. SO_2 was injected throughout the altitude range of 16–25 km at 0° longitude on the equator. The aerosols are radiatively active tracers and are advected within the model via the general circulation. Stratospheric sulfate aerosols injected into the tropical lower stratosphere have an *e*-folding lifetime of approximately 12 months.

2.3. MIROC-ESM-CHEM

MIROC-ESM-CHEM is an Earth System Model (ESM) that has been developed based on a global climate model MIROC (Model for Interdisciplinary Research on Climate) consisting of coupled atmosphere, ocean, sea ice, river, and land surface models. The details of MIROC-ESM-CHEM model and the base (RCP4.5) simulation settings have been documented in Watanabe *et al.* [2011a, 2011b], respectively. The atmosphere model of MIROC-ESM-CHEM has a T42 horizontal resolution (approximately 300 km grid spacing) and contains 80 vertical layers from the surface to a height of about 85 km. The model includes a representation of the solar cycle by specifying a monthly time series of solar spectrum that is binned into model's photochemistry/radiation bands. The QBO is internally calculated using a gravity wave drag parameterization. The El Niño–Southern Oscillation (ENSO) is reproduced by the model's atmosphere–ocean coupled system. The model considers the direct and indirect effects of tropospheric aerosols, while treatments of the stratospheric aerosols are separated from the tropospheric one as outlined below.

In the base simulation, a zonally averaged stratospheric aerosol AOD is provided to the model's radiation module as a function of latitude, altitude, and month following Sato *et al.* [1993], which is exponentially reduced after 1998 with 1 year relaxation time toward a background value of 10^{-4} . In G4, we used similar latitude, altitude, and monthly data of AOD but provided by GeoMIP for models that do not simulate formation of the stratospheric sulfate aerosols from SO_2 gas [Kravitz *et al.*, 2011b]. In radiation calculations, a constant effective radius of 0.237 μm is used for the radiation calculations in both the base and G4 runs. More details of the radiation calculations are discussed by Watanabe *et al.* [2011b].

The atmospheric chemistry module of MIROC-ESM-CHEM predicts the system of tropospheric chemistry (O_x – HO_x – NO_x – CO – CH_4 –VOCs: Volatile Organic Compounds) as well as the major chlorine and bromine compounds (Cl_y and Br_y) that are important for the simulation of stratospheric ozone [Watanabe *et al.*, 2011a]. Parameterizations for liquid and solid particles in the stratosphere are included to calculate heterogeneous reactions on liquid sulfate aerosols (including the hydrolysis of N_2O_5 and BrONO_2) and PSCs [e.g., Carslaw *et al.*, 1995; Hanson and Mauersberger, 1988]. The surface area density (SAD) of PSCs is diagnosed as a function of the predicted temperature and mixing ratio of H_2O and HNO_3 . In this study, on the other hand, the SAD (S) of liquid sulfate aerosols in the stratosphere is given as external forcing. Namely, S (in $\mu\text{m}^2 \text{cm}^{-3}$) is approximately diagnosed in the heterogeneous chemistry package based on the AOD data: $S = 4 c \frac{\Delta\tau}{\Delta z} \frac{1}{\epsilon}$, where c is a constant for unit conversion (10^{10}), $\Delta\tau$ is the AOD in a certain model layer at a certain location, Δz is the model layer thickness in meters, and ϵ is a prescribed constant representing mean efficiency of scattering due to the sulfate aerosols (assumed to be 2). This relationship is derived through a combination of several basic and approximated equations and gives an S distribution which resembles the observations [e.g., Thomason *et al.*, 1997], via solving n and σ from the following: $S = 4\pi \cdot r^2 n$, $\Delta\tau = n\sigma\Delta z$, and $\sigma = \epsilon\pi \cdot r^2$, where n , r , and σ are the number density, effective radius, and a mean scattering cross section of sulfate aerosols in the model layer.

2.4. GEOSCCM

The Goddard Earth Observing System Chemistry Climate Model (GEOSCCM) used for the GeoMIP simulations couples the Goddard Earth Observing System, version 5 (GEOS-5) [Rienecker *et al.*, 2011] general circulation model and the Georgia Institute of Technology–Goddard Global Ozone Chemistry Aerosol Radiation and Transport (GOCART) module [Chin *et al.*, 2000; Colarco *et al.*, 2010], and a stratospheric chemistry module [Pawson *et al.*, 2008].

GEOS-5 uses a finite volume dynamical core [Lin, 2004] combined with a physics package that describes moist processes, radiation, turbulent mixing, and surface processes. Convection is parameterized using the relaxed Arakawa-Schubert (RAS) scheme [Moorthi and Suarez, 1992] and is combined with a prognostic cloud scheme. The boundary layer turbulent mixing is parameterized with the schemes by Louis *et al.* [1982] and Lock *et al.* [2000] for stable and unstable situations, respectively. The land surface model is composed of a catchment-based hydrological model [Koster *et al.*, 2000] and a multilayer snow model [Stieglitz *et al.*, 2001]. The radiative transfer package consists of a solar radiation model [Chou and Suarez, 1999] and a thermal radiation model [Chou *et al.*, 2001]. The solar radiation part includes absorption due to water vapor, O₃, O₂, CO₂, clouds, and aerosols. The thermal radiation module includes absorption by water vapor, CO₂, O₃, and most of the minor trace gases, as well as clouds and aerosols. GOCART includes a parameterization of the chemical production of SO₄ aerosol from oxidation of dimethyl sulfide (DMS) by OH during day and NO₃ during night and from oxidation of SO₂ by OH in the gas phase and by H₂O₂ in the aqueous phase.

GEOSCCM calculates the aerosol surface area density for heterogeneous chemistry from the concentration of SO₄ assuming that the dry stratospheric sulfate aerosol particles are lognormally distributed with modal radius equal to 0.35 μm and standard deviation 1.59. These values have been chosen within the observed range [e.g., Bingen *et al.*, 2004] and result in good agreement with observations after the eruption of Mount Pinatubo [Aquila *et al.*, 2012]. The dry stratospheric aerosol is hydrated depending on the ambient relative humidity following Petters and Kreidenweis [2007].

A similar version of GEOSCCM has been evaluated by Aquila *et al.* [2012, 2013]. With respect to Aquila *et al.* [2013], the version of GEOSCCM used in this work includes the coupling between aerosol and heterogeneous chemistry and an internal mechanism for the generation of the QBO [Molod *et al.*, 2012]. GEOSCCM is used in this work to perform only G4 simulations and the relative control simulations. Here, 5 Tg per year of SO₂ is continuously injected at the equator at 0° longitude. The injection is vertically uniform between 16 km and 25 km altitude. The transformation of SO₂ into sulfate aerosol is calculated by GOCART using climatological oxidant fields [Chin *et al.*, 2000].

2.5. Model Evaluation

Two of the models (ULAQ-CCM and GEOSCCM) that participate in the GeoMIP experiment were extensively evaluated within CCMVal-2 [SPARC-CCMVal, 2010] and, as other CCMVal-2 models, they contributed to the World Meteorological Organization (WMO) assessment of the ozone depletion [WMO/UNEP, 2011]. In general, both models performed well in the stratospheric chemistry evaluation activity and for polar ozone losses. The models did a good job in representing the NO_x/NO_y partitioning in 1993, shortly after the Pinatubo volcanic eruption, while they showed some problems in the ClO_x/Cl_y partitioning. GEOSCCM simulated chemical ozone loss in the Arctic relatively well, while overestimated it in the Antarctic. ULAQ-CCM underestimated Arctic ozone loss for cold Arctic winters and did quite well in the representation of Antarctic ozone loss, as discussed in SPARC-CCMVal [2010, Chapter 6].

GISS-E2-R and MIROC-ESM-CHEM participated in CMIP5 (Coupled Model Intercomparison Project phase 5) in support of the Intergovernmental Panel on Climate Change (IPCC) AR5. The evolution of ozone has been analyzed over the historical (1850–2005) and future (2005–2100) period under the four Representative Concentration Pathways (RCP 2.6, 4.5, 6.0, and 8.5) and revealed a realistic representation of the effects of anthropogenic forcings on stratospheric temperatures and subsequent impacts on tropospheric climate [Eyring *et al.*, 2013]. GISS-E2-R and MIROC-ESM-CHEM also participated in the Atmospheric Chemistry Climate Model Intercomparison Project (ACCMIP), with results presented in Lamarque *et al.* [2013] and in Young *et al.* [2013], the latter for the evolution of tropospheric ozone.

When tested in these intercomparison campaigns, all the above models showed some significant differences in stratospheric transport and some deficiencies that are manifested in the changes in ozone return or other milestone date. In CCMVal-2, for instance, the return date to 1980 values of total ozone column lies just outside the 95% confidence interval of the multimodel mean for the ULAQ-CCM in Antarctic and for GEOSCCM in the Southern midlatitude region, as shown in SPARC-CCMVal [2010, Figure 9.20]. However, the overall behavior of the two models seems to be quite reasonable.

The analysis illustrated here represents a basic selection of diagnostics that reports on the ability of these models to reproduce climatology and trends of the recent past, including a few aspects of the depiction of the

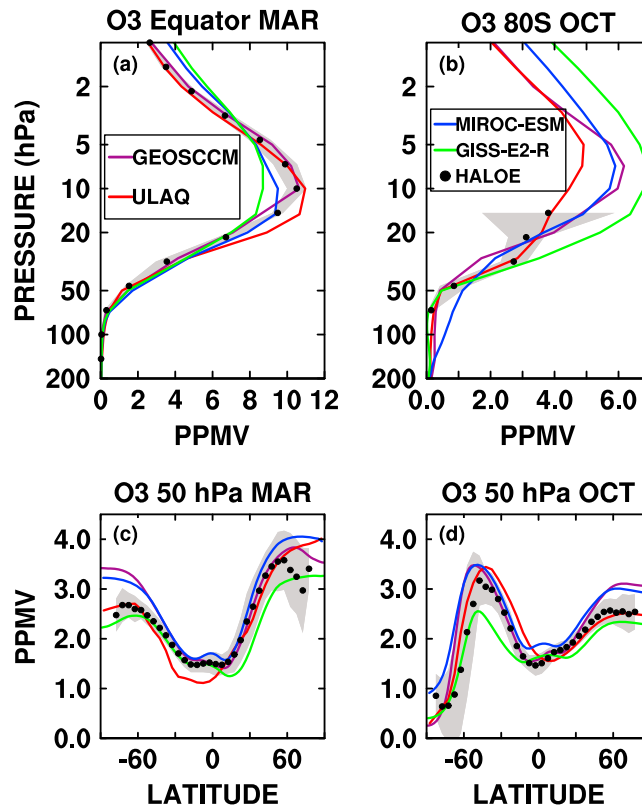


Figure 1. Climatological zonal mean ozone mixing ratios (1991–2002) from the models and HALOE observations (ppmv). (a) Equatorial vertical profile in March, and (b) at 80°S in October. Mixing ratios at 50 hPa as a function of latitude, in (c) March and (d) October. The grey areas shows HALOE $\pm 1\sigma$ of the climatological zonal mean.

whereas GISS-E2-R undervalues ozone depletion between 30 and 20 hPa. This may be in part related to the missing of heterogeneous chemical reduction of NO_x on aerosol SAD.

Figures 2a and 2b compare the 20 year mean climatological total column ozone in March and October (1980–1999) from models and merged satellite data. The satellite data consist of monthly means constructed from individual Total Ozone Mapping Spectrometer (TOMS) and SBUV/2 satellite data sets [Stolarski and Frith, 2006]. All models well represent the main features of the latitudinal profiles. They show the highest ozone values in Northern Hemisphere high latitude spring (Figure 2a), low ozone values in the tropics, a relative ozone maximum in Southern Hemisphere midlatitudes in October, and a minimum ozone column above the Antarctic (Figure 2b). However, in GEOSCCM, Arctic total ozone in March is too high, as well as in Southern Hemisphere midlatitudes, and this is likely related to a strong Brewer-Dobson circulation. Consistently with Figure 1c, MIROC-ESM-CHEM overestimates midlatitude total ozone during Southern Hemisphere spring.

Figure 2c shows the percentage changes of the globally weighted average of the total ozone column, relative to the mean over the period 1971–1980. Model data from 1960 to 2005 are compared to several different observational data sets already used in Eyring *et al.* [2013]. The observations include ground-based measurements (updated from Fioletov *et al.* [2002]), NASA TOMS/OMI/SBUV(2) merged satellite data [Stolarski and Frith, 2006], the National Institute of Water and Atmospheric Research (NIWA) combined total column ozone database [Bodeker *et al.*, 2005], Solar Backscatter Ultraviolet (SBUV, SBUV/2) retrievals (updated from Miller *et al.* [2002]). All the models consistently simulate the negative trend from 1980 to 2000 showing in some cases a strong interannual variability (GISS-E2-R). The four models show an average spread of global ozone changes during the 1990s ranging from 3% (MIROC-ESM-CHEM and ULAQ-CCM) to 6% (GISS-E2-R) and similar to the spread of observations that lies between 4% (Ground-based) and 5% (NASA_TOMS-SBUV-OMI). GISS-E2-R seems to overestimate the reduction of ozone over the period after

past ozone depletion. Figure 1 shows climatological mean vertical profiles of O_3 at different latitudes and months (Figures 1a and 1b) and latitudinal distributions at 50 hPa (Figures 1c and 1d) from all models and measurements. The observations are the climatology between 1991 and 2002 built up from the data of the Halogen Occultation Experiment (HALOE) instrument onboard the Upper Atmosphere Research Satellite (UARS) [Grooss and Russell, 2005]. In the tropical lower stratosphere between 100 and 30 hPa, all models agree well with HALOE observations and lie within the interannual standard deviation (1σ) of the HALOE mean (Figure 1a). Between 30 and 10 hPa, ULAQ-CCM overestimates ozone, whereas GISS-E2-R undervalues the ozone maximum at about 10 hPa. At altitudes above 7 hPa, GEOSCCM and ULAQ-CCM agree well with HALOE data; on the other hand, MIROC-ESM-CHEM and GISS-E2-R slightly overestimate the observations. In the Southern Hemisphere polar spring at 80S (Figure 1b), MIROC-ESM-CHEM is biased high compared to HALOE observations below 50 hPa,

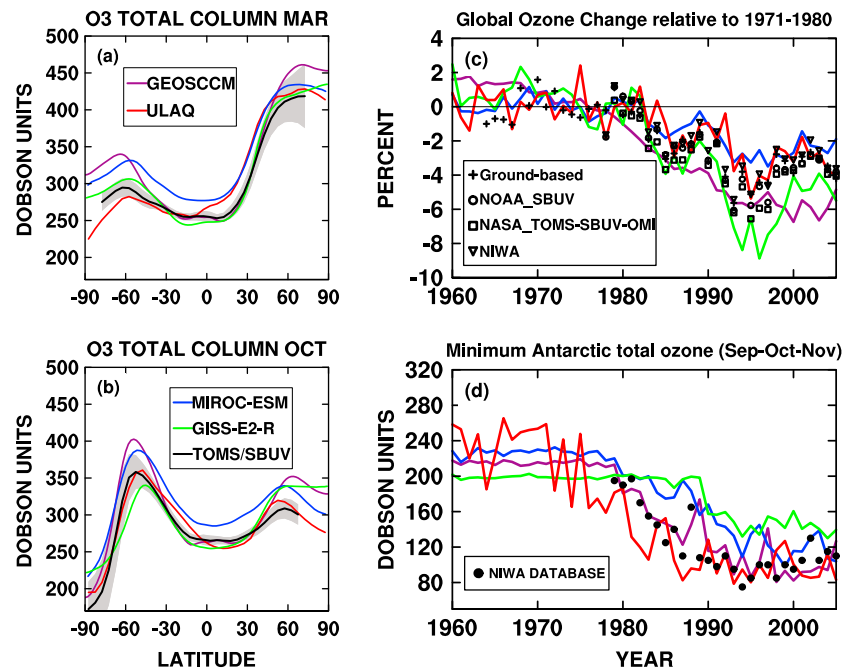


Figure 2. Climatological zonal mean (1980–1999) of total ozone column from the models compared to TOMS/SBUV observations (DU), in (a) March and (b) October. The grey area shows TOMS/SBUV $\pm 1\sigma$ of the climatological zonal mean. (c) Time series of globally and annually averaged total ozone column change relative to the 1971–1980 mean value. Observations from four different sources are shown (see legend and text). (d) Time series of minimum total ozone column for September, October, and November in the Antarctic region (poleward of 60°S). Observations are from NIWA combined total column ozone database.

the Mount Pinatubo eruption in 1992; ULAQ-CCM is following the observed trend rather well and GEOSCCM and MIROC-ESM-CHEM follow the decadal variability and do not show a pronounced decrease of column ozone after volcanic eruptions. One of the ozone indices that have been used in the past to assess the severity of polar ozone depletion is the minimum total ozone column poleward of 60°S. Figure 2d shows the model results for the minimum Antarctic ozone from 1960 to 2005 during September–November, with observations from the NIWA combined total ozone database. ULAQ-CCM and GEOSCCM agree well with observations, whereas MIROC-ESM-CHEM and GISS-E2-R overestimate the minimum values (MIROC-ESM-CHEM up to the mid-1990s).

The above discussion should be intended as a brief overview of the capability of ULAQ-CCM, GEOSCCM, MIROC-ESM-CHEM, and GISS-E2-R to reproduce past ozone observations in the stratosphere and trends. This evaluation and work in earlier assessments indicate that the models perform reasonably well in comparison to past observations, even though some shortcomings in ozone exist, as described above. A full set of diagnostics covering radiation, stratospheric dynamics, transport and chemistry, upper troposphere and lower stratosphere features, natural variability and long-term projections of stratospheric ozone, and stratosphere-troposphere interactions, have been used in previous intercomparison projects developed in the context of WMO activities. These diagnostics enabled the use of the participating models as tools to predict the future evolution of stratospheric ozone and for future sensitivity studies and climate change scenarios, feeding the 2010 WMO ozone assessment [WMO/UNEP, 2011] and the fifth IPCC assessment report [IPCC, 2013].

3. Stratospheric Aerosols

Explosive volcanic perturbations and potential stratospheric sulfate aerosol geoengineering may act as large stratospheric sources of SO₂, producing major transient or steady state increases of the stratospheric sulfate aerosol number, mass, and surface area densities, as well as solar radiation extinction and optical depth; this can result in significant changes of the particle size distribution [Deshler et al., 1992; Thomason

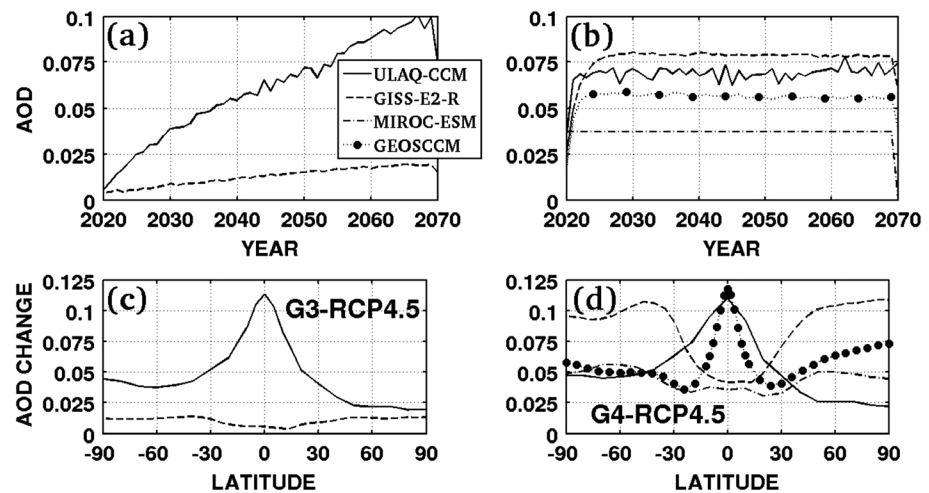


Figure 3. Time series of globally averaged stratospheric AOD at $0.55 \mu\text{m}$ in the models: (a) G3 perturbed case in 2020–2070; (b) G4 perturbed case in 2020–2070; (c) zonally averaged AOD change with respect to RCP4.5 in G3; (d) zonally averaged AOD change with respect to RCP4.5 in G4.

et al., 1997]. These large aerosol perturbations directly impact the radiation budget at the surface and at the top of atmosphere, as well as causing effects on the hydrologic cycle and tropospheric and stratospheric ozone [e.g., Robock, 2000; Robock *et al.*, 2008; Tilmes *et al.*, 2008]. To understand changes in stratospheric ozone due to a perturbation of the stratospheric sulfate aerosol burden, we must first understand how the aerosol size distributions and surface areas change. For example, larger aerosols will have a greater infrared radiative effect with respect to smaller aerosol particles, causing increased stratospheric heating and hence causing greater radiative-chemical-dynamical changes, whereas smaller-sized aerosols scatter more effectively in the short wave and therefore result in a stronger cooling of the Earth's surface. A change in surface area density will change the amount of surface available for heterogeneous chemistry.

Background stratospheric sulfate aerosols are either formed locally by OH oxidation of SO_2 or by upward transport from the troposphere through the tropical tropopause layer (TTL), although the latter process is largely limited by upper tropospheric formation of cirrus ice particles via homogeneous freezing on sulfate aerosols [Hendricks *et al.*, 2011]. Stratospheric SO_2 , in turn, originates either from convection of SO_2 from the boundary layer to the TTL, followed by vertical advection from the TTL or from local photochemical production, following photolysis of carbonyl sulfide [Pitari *et al.*, 2002; Weisenstein *et al.*, 2006]. Sulfuric acid produced at the end of the SO_2 oxidation chain forms aerosol particles via homogeneous nucleation and, to a lesser extent, via heterogeneous nucleation of carbonaceous particles transported from the troposphere. The particle size distribution is determined by these and other microphysical processes, such as condensational growth, coagulation, gravitational settling, and evaporation in the upper stratosphere. The main sink for stratospheric sulfate aerosols is the middle-high latitude downward transport toward the troposphere coupled to gravitational sedimentation.

Model predictions of AOD perturbations in the GeoMIP experiments are presented in Figures 3a and 3b, for G3 and G4, respectively. G4 imposes the amount of SO_2 injected mass flux (5 Tg/year): intermodel differences arise from longer or shorter stratospheric aerosol lifetimes, which in turn are produced by intermodel differences of the tropical pipe isolation and net mixing with extratropics, as well as differences of the Brewer-Dobson circulation strength and its potential modulation by stratospheric aerosol heating and QBO. The aerosol particle size distribution also plays an important role, by affecting the gravitational sedimentation rate and the aerosol optical properties. On the other hand, G3 imposes the conservation of the top-of-atmosphere radiative forcing (TOARF) during the GeoMIP time span (2020–2070). Assuming that the net change of the TOARF in these 50 years is of the order of 2 W/m^2 [Meinshausen *et al.*, 2011], the imposed stratospheric mass flux of SO_2 in G3 may have large variations among the models. This depends mostly on the treatment of the aerosol effects on other atmospheric processes (e.g., O_3 , tropospheric

cloudiness, and albedo), since the direct aerosol equivalent-albedo effect is only slightly affected by the model-predicted aerosol size [Lacis *et al.*, 1992]. In the present study, G3 with interactive ozone is simulated by two models (ULAQ-CCM and GISS-E2-R), both of which include explicit aerosol feedbacks with ozone photochemistry, in particular dynamical feedbacks and changes in the photolysis rates. Model predicted aerosol optical depth for G3 is approximately a factor of 5 larger in ULAQ-CCM than GISS-E2-R, which results in larger aerosol feedbacks in ULAQ-CCM, including stronger radiative heating, tropical updraft, and changes in transport. ULAQ-CCM requires a larger amount of aerosol burden to balance surface temperatures than the GISS-E2-R model, in part due to a low responsiveness of GISS-E2-R to CO₂ changes and therefore low climate sensitivity as compared to several other models participating in CMIP5 [e.g., Kravitz *et al.*, 2013]. The two models agree quite well in the predicted globally averaged AOD in G4, where the SO₂ mass flux is imposed independent of its net effect on the radiative forcing.

Figures 3c and 3d show that the AOD latitudinal dependence is rather different among models that predict aerosols from the SO₂ injection: GEOSCCM and ULAQ-CCM have similar aerosol effective radii (Table 2) and then comparable stratospheric aerosol loss due to sedimentation. This, coupled to a good tropical pipe isolation [e.g., Strahan *et al.*, 2011; Chipperfield *et al.*, 2013], produces an effective aerosol confinement in the tropics, with a clear equatorial AOD maximum and comparable globally averaged AOD. On the other hand, the GISS-E2-R latitudinal distribution shows a much faster aerosol dispersion toward middle-high latitudes (associated with a more efficient subtropical horizontal air mixing in the lower stratosphere), thus producing a tropical minimum of the AOD. The globally averaged value, however, is comparable and even higher than that of GEOSCCM and ULAQ-CCM, due to the slower sedimentation loss produced by the smaller particle size (Table 2). The latitudinal behavior of AOD in MIROC-ESM-CHEM (prescribed) is qualitatively similar to that of GISS-E2-R, with a minimum at the tropics, but with a smaller latitudinal gradient.

The growth of stratospheric aerosol particles, produced by both transient and sustained SO₂ injections, modifies the particle size distribution shape leading to significantly larger effective radii with respect to normal background conditions of the stratosphere. This is highlighted both in direct satellite measurements of aerosol extinction after a major volcanic eruption [Thomason *et al.*, 1997] and in global modeling studies [Weisenstein *et al.*, 2006; Heckendorn *et al.*, 2009; English *et al.*, 2012]. Because of their large size, these particles have a reduced albedo and a faster sedimentation rate, with a net reduction of the stratospheric lifetime: both effects limit the cooling potential in comparison to stratospheric background aerosols. In addition, the increasing particle size favors the absorption of infrared radiation both in the solar NIR and planetary spectra, leading to larger additional tropical heating rates. This local radiative perturbation may have a potential increasing impact on tropical upwelling and (by continuity) on the extratropical downwelling, acting again to reduce the lifetime of stratospheric aerosols. Table 2 shows that two of the three models that form aerosols from the stratospheric SO₂ injection actually predict an increase of the effective radius in G4 with respect to RCP4.5 (i.e., ULAQ-CCM and GISS-E2-R), and two models calculate a G4 perturbed effective radius close to SAGE-II observations after the Pinatubo eruption (ULAQ-CCM and GEOSCCM). The effective radius is the radiative-effective aerosol dimension, determining the efficiency of radiation scattering and absorption. Intermodel differences in Table 2 need to be taken into account to evaluate the GeoMIP aerosol impact on radiative processes, such as photolysis, stratospheric heating rates, tropopause forcing, and UV transmittance.

The combination of total stratospheric AOD, effective radius, and latitudinal distribution of the particles produces the final net radiative impact of geoengineering aerosols, as summarized in Table 3. This table and the following ones report the “adjusted tropopause RF,” which is the radiative forcing (RF) definition we refer throughout the paper [Hansen *et al.*, 2005]. The globally averaged net adjusted tropopause RF of the aerosols scales with the AOD; the RF/AOD ratio (i.e., the “normalized forcing”) ranges from 23 to 22.7 of ULAQ-CCM and GEOSCCM to 19.7 and 17.5 of MIROC-ESM-CHEM and GISS-E2-R, respectively. The models with a stronger tropical confinement of the aerosols, coupled to an effective radius comparable to that observed in post-Pinatubo conditions (i.e., ULAQ-CCM and GEOSCCM) calculate a normalized forcing close to that reported in Hansen *et al.* [2005] for a Pinatubo experiment (24). A similar model behavior is also found for globally averaged percent changes of surface UV-B (last column in Table 3): these values, normalized to the AOD, range from 21.6% to 21% in ULAQ-CCM and GEOSCCM and from 15% to 11.2% in MIROC-ESM-CHEM and GISS-E2-R, respectively.

Table 3. Aerosol Optical Depth Changes With Respect to Base Case ($\lambda=0.5\ \mu\text{m}$); Shortwave, Longwave, Adjusted Longwave and Net Adjusted Tropopause Radiative Forcing of Stratospheric Sulfate Aerosols; Surface UV-B Percent Change Due Only to Stratospheric Aerosols^a

	AOD	RF-Aerosol SW (W/m ²)	RF-Aerosol LW (W/m ²)	RF-Aerosol LWadj (W/m ²)	RF-Aerosol Net (W/m ²)	UV-B Change (%)
G4 – RCP4.5	0.067	−2.09	0.24	0.55	−1.54	−1.45
ULAQ-CCM						
G4 – RCP4.5	0.037	−1.00	0.18	0.27	−0.73	−0.55
MIROC-ESM-CHEM						
G4 – RCP4.5	0.056	−1.72	0.21	0.45	−1.27	−1.17
GEOSCCM						
G4 – RCP4.5	0.075	−1.91	0.41	0.60	−1.31	−0.84
GISS-E2-R						
G3 – RCP4.5	0.060	−1.87	0.22	0.49	−1.38	−1.32
ULAQ-CCM						
G3 – RCP4.5	0.010	−0.24	0.05	0.07	−0.17	−0.09
GISS-E2-R						

^aValues shown are annually and globally averaged for the whole decade 2040–2049. Radiative calculations are made off-line at the tropopause in all-sky conditions with a well-tested radiative transfer code [Chou and Suarez, 1999; Chou et al., 2001], using as input the gridded distributions from different models and experiments; the stratospheric temperature adjustment is based on each model individual profile and is performed leaving the tropospheric temperature profile unchanged, as in Hansen et al. [2005, Figure 2b].

The SAGE-II measured extinction ratio between visible and NIR wavelength channels (i.e., 0.525 and 1.02 μm , respectively) is a good measure of the aerosol size distribution shape and its modifications produced by changes in the local sulfate productions rate from OH oxidation of SO₂ [Weisenstein et al., 2006]. As shown in Figure 4, this ratio is close to unity when the effective radius (r_{eff}) is close to 0.6 μm and about 3 for $r_{\text{eff}}=0.2\ \mu\text{m}$. The ULAQ-CCM is the only model included in this paper with explicit aerosol microphysics and calculates the time behavior of the sulfate aerosol size distribution as a function of stratospheric SO₂, OH, and large-scale transport. Its predictions in terms of the extinction ratio (and hence of the aerosol size distribution shape) are shown in Figure 4 to be in good agreement with SAGE-II observations, for both background and perturbed conditions (G4 and Pinatubo). Figure 4b compares directly the ULAQ-CCM calculations of the aerosol size distribution for background and G4 conditions, confirming previous findings [e.g., English et al., 2012].

Aerosol SAD changes are important for assessing changes in heterogeneous reactions in the stratosphere, and therefore changes in the abundance of NO_x and other O₃ destroying substances (Cl_x, Br_x). The models

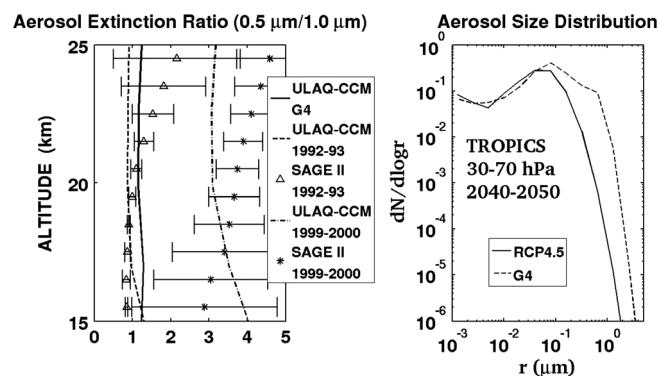


Figure 4. (a) Vertical profiles of aerosol extinction ratio between 0.525 μm and 1.020 μm wavelength channels in the tropics (20°S–20°N), as calculated in the ULAQ-CCM for case G4 (solid line, 2040–2049 average), for the Pinatubo case (dashed line, July 1992–June 1993), and for background conditions (dash-dotted line, 1999–2000), compared to SAGE II retrievals (triangles and asterisks for 1992/1993 and 1999/2000 conditions, respectively). (b) Aerosol size distribution ($dN/d\log r$, cm^{-3}) calculated in the ULAQ model and averaged over the tropics and in the 30–70 hPa vertical layer (2040–2049). Solid line is for RCP4.5; dashed line is for G4.

use different approaches for calculating the SAD. ULAQ-CCM calculates directly the geometric surface area starting from the predicted aerosol size distribution. GEOSCCM calculates the SAD from the sulfate aerosol mass concentration, assuming that the dry stratospheric sulfate aerosol is lognormally distributed with modal radius 0.35 μm and standard deviation 1.59. This dry size distribution is hydrated depending on the relative humidity following Petters and Kreidenweis [2007]. MIROC-ESM-CHEM approximately calculates the SAD from the prescribed AOD distribution, as mentioned in section 2.3.

Model results for SAD are evaluated with SAGE-II data, for both volcanically quiet

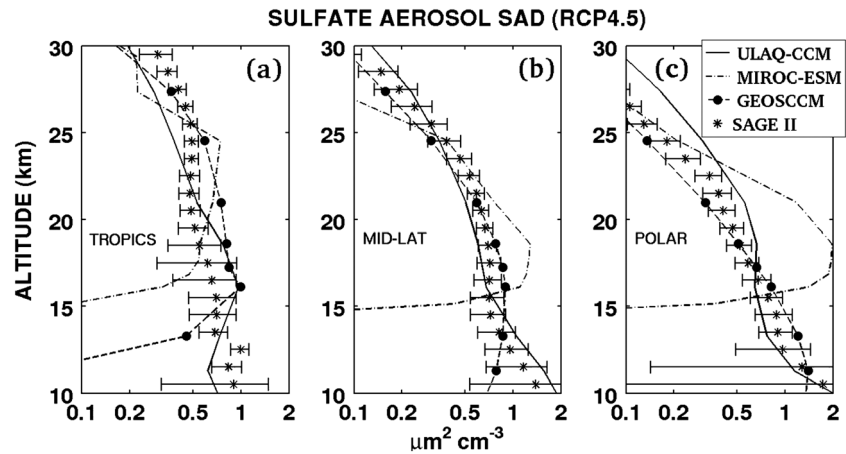


Figure 5. Sulfate aerosol surface area density ($\mu\text{m}^2/\text{cm}^3$) calculated in the models ULAQ-CCM, MIROC-ESM-CHEM, and GEOSCCM for background conditions (1999–2000 average) and compared to SAGE-II data (asterisks). (a) Tropics (20°S – 20°N), (b) midlatitudes (30°S – 50°S , 30°N – 50°N), and (c) polar regions (60°S – 90°S , 60°N – 90°N).

(Figure 5) and perturbed conditions (Figure 6). Although some differences are present in the latitudinal distribution of the aerosol SAD, the three models are roughly consistent with the reported SAGE-II derived SAD values for background and post-Pinatubo conditions, except for MIROC-ESM-CHEM values below 16 km altitude and for the background high-latitude values. The average sulfate mass loading above the tropopause in G4 steady state conditions (2.82 ± 0.02 Tg-S, 13.5 months average lifetime) is comparable with respect to July 1992–June 1993 post-Pinatubo conditions (2.76 ± 0.05 Tg-S, 11 months *e*-folding time). These mass burden estimates are calculated as an average from ULAQ-CCM and GEOSCCM time-dependent simulations. This makes it possible and meaningful to use the indirect G4 SAD evaluation with SAGE-II derived values from July 1992 to June 1993. On average, the three models show a factor 12–25 increase of the tropical aerosol SAD at 50 hPa with respect to RCP4.5 (with ULAQ-CCM at the upper limit), and a factor 3–10 increase at middle-high latitudes (with GEOSCCM at the lower limit). These large sulfate aerosol SAD increases greatly affect the stratospheric NO_x - HO_x - Cl_x - Br_x chemistry [Fahey *et al.*, 1993] by converting more NO_x into HNO_3 and by increasing the amount of HO_x and reactive Cl-Br. The balance of these catalytic ozone-destroying cycle

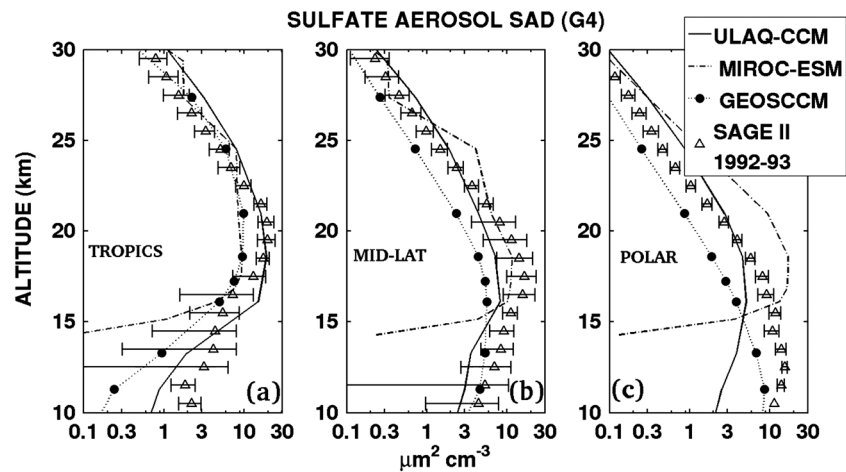


Figure 6. As in Figure 5 but for case G4 (2040–2049 average). An indirect comparison is made with SAGE-II data for post-Pinatubo conditions (July 1992–June 1993 average; triangles). The average sulfate mass loading above the tropopause is comparable in the latter case with respect to G4. The stratospheric mass burden comparison in these two cases is made using averages from ULAQ-CCM and GEOSCCM time-dependent simulations (2.76 ± 0.05 Tg-S for July 1992–June 1993 post-Pinatubo conditions and 2.82 ± 0.02 Tg-S for G4 in 2040–2049). Gaps in SAGE-II data below 21 km altitude at tropical latitudes are found during July 1992: these gaps are filled by extrapolating SAD values downward into the region with missing data.

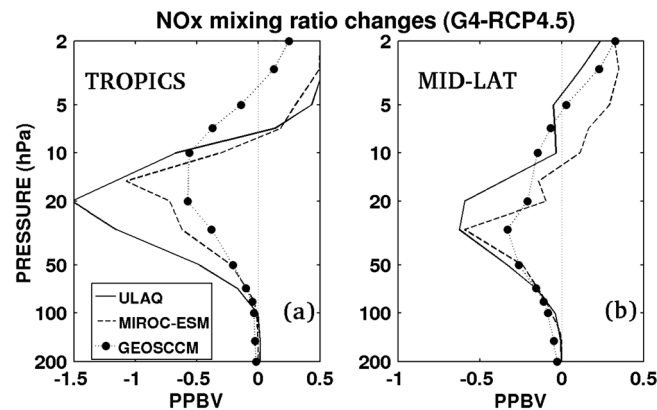


Figure 7. Annual mean of NO + NO₂ mixing ratio changes, as calculated in ULAQ-CCM, MIROC-ESM-CHEM, and GEOSCCM (2040–2049).

changes may enhance or limit the stratospheric ozone destruction depending on latitude, altitude, and on the (time-dependent) total stratospheric amount of inorganic Cl_y and Br_y.

4. Stratospheric Ozone

The increase in stratospheric sulfate concentrations affects ozone via enhancement of heterogeneous chemistry [e.g., Brasseur and Granier, 1992], changes in photolysis rates due to the increased aerosol optical thickness [Kinne et al., 1992], and

modifications of the atmospheric dynamics due to aerosol-ozone perturbations of the stratospheric heating rates [Pitari and Rizzi, 1993; Aquila et al., 2013], which are coupled to altered amplitude and propagation of planetary waves [Pitari and Mancini, 2002]. The temperature perturbations in the middle stratosphere may also affect the homogeneous chemical reaction rates with pronounced temperature dependence, such as O + O₃ and NO + O₃. ULAQ-CCM and MIROC-ESM-CHEM include all of these effects. GEOSCCM includes the ozone perturbations due to heterogeneous and homogeneous chemistry and to atmospheric dynamics, but not changes in photolysis rates. GISS-E2-R includes the ozone perturbations due to changes in photolysis rates, atmospheric dynamics, and homogeneous chemistry but not those due to heterogeneous chemistry on the sulfate aerosol surface. However, GISS-E2-R does include treatments of heterogeneous chemistry in polar stratospheric clouds, which is particularly relevant for Antarctic ozone changes.

The models consistently simulate an enhancement of the heterogeneous chemical reactions in the GeoMIP experiments, with a direct significant reduction of stratospheric NO_x, as observed after major volcanic eruptions [e.g., Johnston et al., 1992; Fahey et al., 1993; Koike et al., 1994]. Figure 7 shows the NO_x (NO + NO₂) mixing ratio changes for G4 during the central decade 2040–2049 (GISS-E2-R is not pictured in Figure 7 because it does not include heterogeneous chemistry on the particle surfaces). All models calculate a decrease in NO_x between 100 hPa and 5 hPa altitude in the tropics (20°S–20°N) and midlatitudes (30°S–50°S and 30°N–50°N) of the order of 0.5–1 ppbv in the 50–10 hPa layer. Above 10 hPa, the models show a small increase of NO_x (0.2 to 0.5 ppbv at 2 hPa). This is primarily due to the fact that both O₃ and NO₂ photolysis increase as a consequence of the aerosol scattering. Hence, the NO/NO₂ ratio increases and less NO₂ is available as sink for NO_x into HNO₃ (via NO₂ + OH). This effect is less evident in GEOSCCM, which does not take into account the aerosol impact on photolysis. Note that the effect of the enhanced heterogeneous chemistry on ozone concentrations is time-dependent. Thanks to the Montreal Protocol, the atmospheric concentrations of chlorine are expected to decrease. Hence, the ozone depletion due to increased ClO_x chemistry in the lower stratosphere is expected to become less and less important with respect to the ozone increase due to the suppression of the NO_x ozone-depleting cycle at higher altitudes.

4.1. Changes in the Vertical Profile of Ozone and Model Evaluation

A comparison of O₃ production/loss terms per chemical family in G4 with respect to the base case has been made with the ULAQ model output. To highlight the direct impact of the changes of different ozone destroying cycles on ozone, the net chemical production term (P-L[O₃]) has been compared with the two simulations by keeping [O₃] fixed at the RCP4.5 value, which means that a comparison of O₃ production (P) and loss frequency (L) terms is actually made (ΔP and [O₃] · ΔL are plotted in Figure 8). The ULAQ-CCM calculates an increase in net ozone production rate in the tropics between 30 hPa and 7 hPa for the decade 2040–2049 (on average +0.2 · 10⁵ cm⁻³ s⁻¹) and a decrease at all other tropical stratospheric altitudes (Figure 8a). Chemical ozone changes are most significantly impacted by the strong reduction of the NO_x cycle, resulting in a net increase of the ozone production term from the NO_x cycles up to about 7 hPa (with a peak increase of +1.5 · 10⁵ cm⁻³ s⁻¹ at 20 hPa). At the same altitudes HO_x, Cl_x, and Br_x loss rates are increased

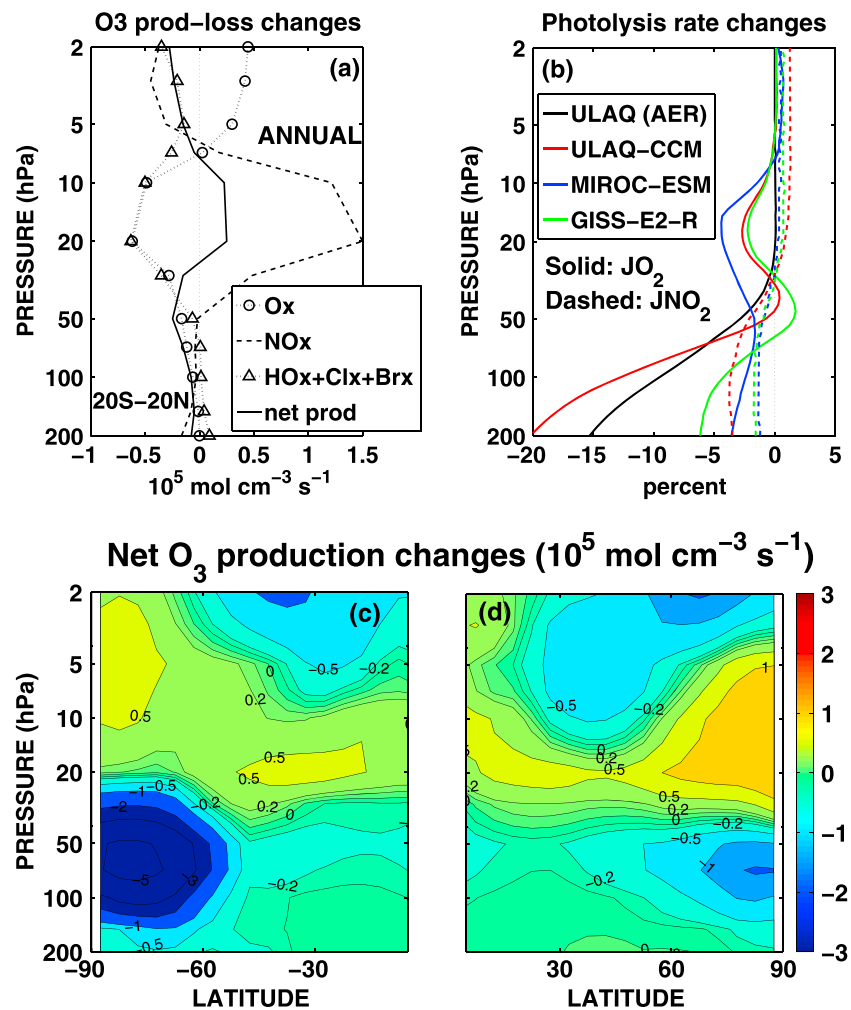


Figure 8. (a) Changes of net ozone production terms per family ($10^5 \text{ mol cm}^{-3} \text{ s}^{-1}$) in G4 with respect to RCP4.5 (2040–2049), as calculated in the ULAQ-CCM (tropics, annual mean); see legend for the different curves. (b) Calculated percent changes of O_2 and NO_2 photodissociation coefficients in G4 with respect to base case (tropics, spring equinox) for those models including the aerosol scattering feedback on photolysis rates; see legend for the different curves. The solid black line shows the JO_2 perturbation in the ULAQ model with only aerosol changes taken into account in G4, while O_3 is kept fixed at RCP4.5 values in order to evaluate the photodissociation sensitivity to the aerosol perturbation alone. (c,d) Zonally and monthly averaged changes of net ozone production ($10^5 \text{ mol cm}^{-3} \text{ s}^{-1}$) in G4 with respect to RCP4.5 (2040–2049) as calculated in the ULAQ-CCM for October and March, respectively.

[Solomon, 1999] ($-0.6 \cdot 10^5 \text{ cm}^{-3} \text{ s}^{-1}$ at 20 hPa), resulting in a net increase of ozone production, in agreement with earlier results [Tilmes et al., 2009; Heckendorn et al., 2009].

The perturbation to the O_2 photolysis rate (see Figure 8b) dominates below 50 hPa due to the UV screening effect by the aerosols. Results from the three models with aerosol scattering impact on photolysis rates are all consistent, with a JO_2 reduction at 70 hPa ranging from 2 to 7%, depending on changes of aerosol optical depth and effective radius. The ozone increase forced by the NO_x cycle perturbation in the 7–30 hPa layer has a feedback on the O_2 photolysis (Figure 6b), thus decreasing the O_3 production from JO_2 in this same layer ($-0.5 \cdot 10^5 \text{ cm}^{-3} \text{ s}^{-1}$, on average), as can be seen in the reduction of the O_x rates. Changes of ozone production/loss above 7 hPa ($-0.2 \cdot 10^5 \text{ cm}^{-3} \text{ s}^{-1}$, on average) result from partially compensating effects of slightly increasing JO_2 and decreasing $\text{O}(\text{^3P})$ from O_3 photolysis on one side and increasing NO_x on the other side (Figure 7).

Figures 8c and 8d show the latitude-altitude distribution of October and March averaged changes of ozone net production in the Southern and Northern Hemispheres respectively. The layer of increased ozone net production above 30 hPa is due to the suppression of the NO_x cycle [Tie and Brasseur, 1995]. The large

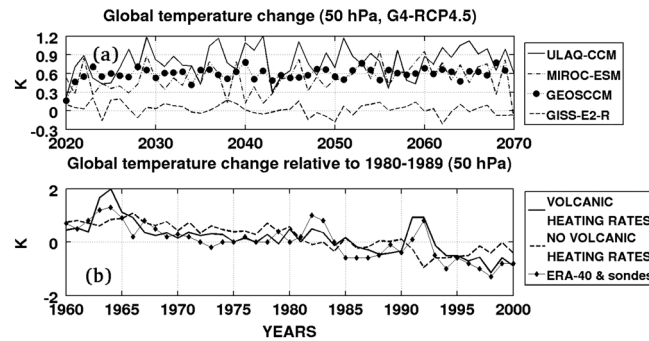


Figure 9. (a) Time series of model calculated global temperature changes (G4-RCP4.5) at 50 hPa from 2020 to 2070 (K). (b) As in Figure 9a but for ULAQ-CCM temperature anomalies from 1960 to 2000 relative to the 1980–1989 average, compared to observations. Solid/dashed lines are with/without volcanic aerosol stratospheric heating, respectively. Observations are from sondes and ERA-40 reanalysis (solid line with diamonds) [Eyring et al., 2006].

impact of additional Cl-Br activation is evident at the location of both Antarctic and Arctic vortices (up to $-5.0 \cdot 10^5 \text{ cm}^{-3} \text{ s}^{-1}$ and $-1.5 \cdot 10^5 \text{ cm}^{-3} \text{ s}^{-1}$, respectively) due to the NO_x reduction produced by the increased aerosol SAD and by increasing Cl_x and Br_x , diabatic cooling, and enhanced formation of PSCs as a consequence of the local temperature decrease, with a positive feedback on ozone loss frequencies [Tilmes et al., 2009]. This appears to be the largest chemical impact of geoengineering aerosols on stratospheric ozone. Negative changes above 7 hPa are produced by coupled changes of NO_x (Figure 7) and O_2 photolysis (Figure 8b).

In the tropics, an important proportion of the ozone anomaly produced by sulfate geoengineering is caused by changes in upwelling due to perturbations of stratospheric heating rates [Tilmes et al., 2009]. The heating from sulfate aerosols in the tropical middle stratosphere produces a temperature increase, which is mitigated by the ozone depletion below 30 hPa. Anomalies of the global temperature at 50 hPa are shown in Figure 9a. GISS-E2-R simulates the smallest temperature anomaly. This is consistent with the smaller particle radius assumed in GISS-E2-R (see Table 2), which results in lower heating rates due to the smaller infrared absorption [Niemeier et al., 2011]. It is also consistent with larger ozone depletion, hence cooling, due to the larger change in UV scattering and O_2 photolysis and to the absence of heterogeneous chemistry on sulfate aerosols (see ahead). Table 4 shows that all models calculate a small change of tropical temperatures at 100 hPa, i.e., at the entry point of stratospheric air. GEOSCCM simulates the highest temperature anomaly in G4 (0.58 K), followed by ULAQ-CCM (0.41 K), MIROC-ESM-CHEM (0.16 K), and GISS-E2-R, which in turn shows a cooling (-0.45 K), consistent with the larger tropical O_3 depletion in this model. As shown in Table 4, the TTL warming ends up producing in G4 an average stratospheric H_2O increase of 0.35 and 0.22 ppmv in the case of GEOSCCM and ULAQ-CCM, respectively, whereas the corresponding changes for the other two models are smaller or negative (0.02 and -0.36 ppmv , for MIROC-ESM-CHEM and GISS-E2-R, respectively). For GEOSCCM and ULAQ-CCM, the stratospheric water vapor increase leads to infrared stratospheric cooling rates and to a positive radiative forcing (see Table 4), partially balancing the effect of the geoengineering aerosol.

Table 4. Temperature Changes at the TTL (100 hPa, 15°S – 15°N)^a

	T (K) 100 hPa 15°S – 15°N	H_2O (ppmv)	RF- H_2O SW (mW/m^2)	RF- H_2O LW (mW/m^2)	RF- H_2O LWadj (mW/m^2)	RF- H_2O Net (mW/m^2)
G4 – RCP4.5	0.40	0.22	–6.7	68.9	55.9	49.2
ULAQ-CCM	0.41	0.22	–6.7	68.9	55.9	49.2
G4 – RCP4.5	0.16	0.02	–0.5	7.5	4.2	3.7
MIROC-ESM-CHEM	0.16	0.02	–0.5	7.5	4.2	3.7
G4 – RCP4.5	0.58	0.35	–10.8	107	88.0	77.2
GEOSCCM	0.58	0.35	–10.8	107	88.0	77.2
G4 – RCP4.5	–0.45	–0.36	11.5	–118	–102	–90.5
GISS-E2-R	–0.45	–0.36	11.5	–118	–102	–90.5
G3 – RCP4.5	0.20	0.12	–3.6	38.3	30.4	26.8
ULAQ-CCM	0.20	0.12	–3.6	38.3	30.4	26.8
G3 – RCP4.5	–0.03	–0.03	1.1	–8.2	–9.6	–8.5
GISS-E2-R	–0.03	–0.03	1.1	–8.2	–9.6	–8.5

^aGlobally averaged values of the following: stratospheric H_2O mixing ratio changes with respect to base case; short-wave, longwave, adjusted longwave, and net adjusted tropopause radiative forcing of water vapor. Values shown are annually averaged for the whole decade 2040–2049. RF values are calculated as in Table 3.

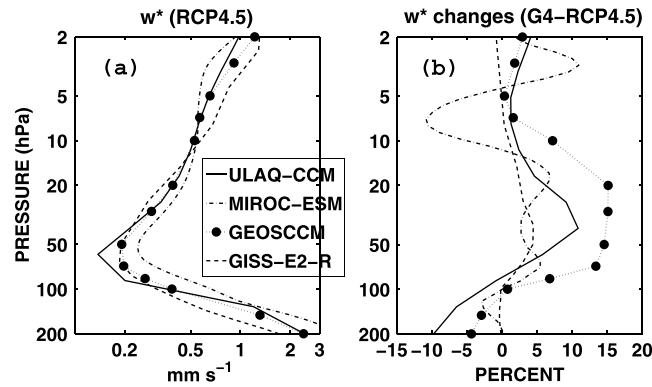


Figure 10. Annual mean of model calculated residual vertical velocity w^* in the tropical stratosphere (mm/s) (average 15°S – 15°N , 2040–2049) for baseline conditions in Figure 10a and percent changes of G4-RCP4.5/RCP4.5 in Figure 10b.

Furthermore, the higher water mixing ratio may enhance the HO_x cycle for ozone destruction [Heckendorn et al., 2009].

Figure 9b shows the historical globally averaged temperature anomalies from 1960 to 2000, with respect to the 1980–1989 average temperature. Observed anomalies during the years perturbed by major volcanic eruptions (i.e., Agung, El Chichón, and Pinatubo) are comparable in magnitude with the model predictions in Figure 9a. The ULAQ-CCM model results including the stratospheric heating from volcanic aerosols are in good agreement with sondes observations and ERA-40

reanalysis. In particular, the stratospheric warming after the 1991 eruption of Mount Pinatubo is well simulated, while the observed temperature increase at 50 hPa during 1991–1992 is absent in the simulation not including volcanic aerosol heating rates.

Figure 10 shows the simulated residual vertical velocity (w^*) in the base case and its anomaly in G4 with respect to the base case. The models show a good consistency in the tropical upwelling and in the overall qualitative behavior of the G4 anomaly profile, with the magnitude of the largest relative increase of w^* between 20 and 30 km altitude, ranging from 2 to 5% for GISS-E2-R and MIROC-ESM-CHEM on one side, and from 5 to 15% for ULAQ-CCM and GEOSCCM on the other side. Increase of the tropical upwelling after major explosive eruptions is reported in several modeling studies, along with significant diabatic heating rates in the tropical stratosphere [e.g., Pitari and Rizi, 1993; Stenichkov et al., 1998; Aquila et al., 2013]. A study of Dunkerton and Delisi [1991] on the stratospheric dynamical perturbations during 1982/1983 (after the El Chichón eruption) shows how anomalies of temperature and zonal winds in the upper stratosphere could be explained as a consequence of the adiabatic cooling taking place in the tropical stratosphere due to the increased upwelling. An indirect proof of the enhanced tropical upwelling can be found in the observed substantial loss of ozone above the TTL after the Pinatubo eruption [Grant et al., 1992]. The pronounced modification of the stratospheric tropical ozone profile is largely driven by the increasing upwelling of ozone poor air to ozone rich regions. Bottom line reasons for the different model response in terms of additional tropical upwelling might be, among others, different climate sensitivity, interactive versus prescribed SSTs, different parameterizations of the aerosol

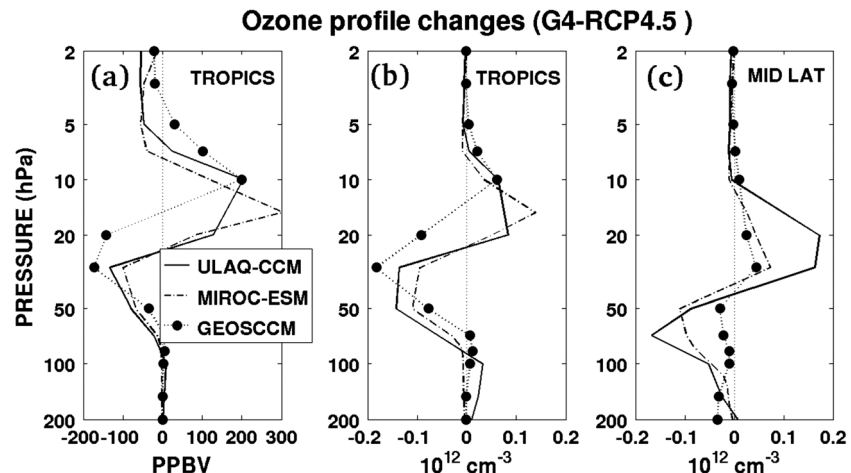


Figure 11. Calculated annual mean of ozone profile changes in G4 with respect to base case (2040–2049). (a) Tropical mixing ratio (ppbv). (b) Tropical number concentration (10^{12}cm^{-3}). (c) Midlatitude number concentration (10^{12}cm^{-3}).

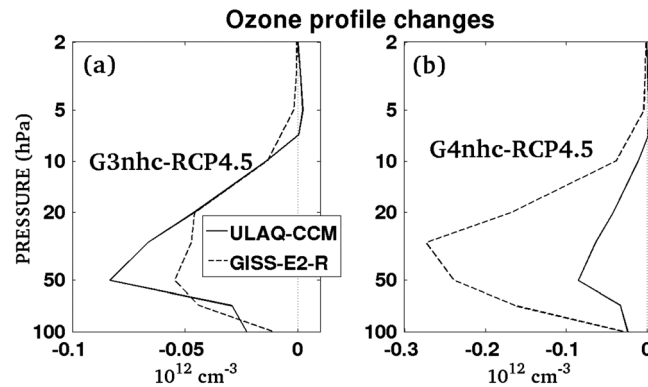


Figure 12. As in Figure 11b but for (a) G3 and (b) G4, both without heterogeneous chemistry on sulfuric acid aerosols.

radiative properties, aerosol size distribution, tropical aerosol concentration, the latter produced by different sedimentation rates and tropical confinement.

Figure 11 shows the vertical profiles of ozone changes in G4 at the tropics and midlatitudes, as simulated by ULAQ-CCM, MIROC-ESM-CHEM, and GEOSCCM; GISS-E2-R results are discussed separately (Figure 12), as this model does not include the effects of changing NO_x chemistry on the enhanced sulfate aerosol SAD. In the tropical region (Figures 11a and 11b),

ULAQ-CCM and MIROC-ESM-CHEM predict a decrease of ozone between 100 hPa and 50 hPa mostly due to the decrease in O₂ photolysis (Figure 8b). GEOSCCM simulates no change below 70 hPa, as the aerosol feedback on photolysis rates is absent in this model. From 70 to 30 hPa, the ozone changes due to increased upwelling (Figure 10) contribute to the total ozone anomaly together with the enhanced chemical loss in HO_x, Cl_x and Br_x chemical cycles (Figure 8a), creating the maximum negative ozone anomaly visible at 30 hPa (−150 ppbv on average). Above 30 hPa the suppression of the NO_x cycle dominates the chemical perturbation (about +200 ppbv at 10 hPa), with GEOSCCM showing a wider altitude range of the negative ozone anomaly, due to the larger increase of upwelling in this model (Figure 10). At midlatitudes (Figure 11c), where the effect on ozone of the increased upwelling disappears and the changes due to photolysis and heterogeneous chemistry dominate, GEOSCCM simulates smaller ozone anomalies with respect to ULAQ-CCM and MIROC-ESM-CHEM.

The ozone tropical changes in GISS-E2-R are compared to ULAQ-CCM (run in this case without heterogeneous chemistry on sulfate aerosols) in Figure 12. Figure 12a shows the ozone anomalies in G3: the smaller aerosol particles in GISS-E2-R with respect to ULAQ-CCM (Table 2) scatter more UV radiation, increasing the O₂ photolysis. This effect, however, is balanced by the lower AOD calculated by GISS-E2-R (Figure 3) and results in an ozone anomaly vertical profile similar to ULAQ-CCM nhc. In G4 (Figure 12b), where the sulfate injection burden is fixed by the experiment design, the AOD simulated by GISS-E2-R and ULAQ-CCM is similar, and the net results is a 5 times larger ozone depletion in GISS-E2-R than in ULAQ-CCM.

All models with heterogeneous chemistry simulate a significant increase in ozone depletion in the Antarctic region, due to a combination of increasing sulfate aerosol SAD and enhanced formation of PSCs produced in turn by local adiabatic and nonadiabatic cooling (Figure 13a), the latter due to the feedback of photochemical ozone losses. ULAQ-CCM predicts the largest increase in springtime ozone depletion (Figure 13b) (−300 ppbv at 50 hPa). GEOSCCM simulates a different SAD profile change at polar latitudes (Figure 6c), resulting in different

temperature anomalies and the smallest ozone depletion at 50 hPa during October. A larger ozone loss, on the other hand, is predicted in this model below 100 hPa layer, consistently with the SAD change. GISS-E2-R, which does not include heterogeneous chemistry on the surfaces of the aerosols, still includes a parameterization of ozone depletion via interactions with polar stratospheric clouds. The missing heterogeneous chemical reduction of NO_x on aerosol SAD does not allow in this model a limitation of the ozone loss above 50 hPa (Figure 13b). This ozone

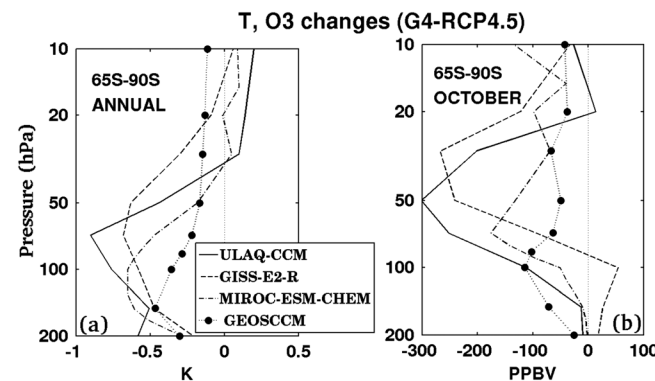


Figure 13. G4-RCP4.5 changes averaged over the South Polar region (65°S–90°S) for 2040–2049. (a) Annual mean temperature (K); (b) October mean ozone mixing ratio (ppbv).

Table 5. O₃ Column Changes With Respect to Base Case; Shortwave, Longwave, Adjusted Longwave, and Net Adjusted Tropopause Radiative Forcing of Ozone; Surface UV-B Percent Change Due Only to Ozone^a

	O ₃ Column (DU)	RF-O ₃ SW (mW/m ²)	RF-O ₃ LW (mW/m ²)	RF-O ₃ LWadj (mW/m ²)	RF-O ₃ N (mW/m ²)	UV-B Change (%)
G4 – RCP4.5	-1.1	2.0	-16.5	-34.1	-32.1	0.40
ULAQ-CCM						
G4 – RCP4.5	-1.1	8.8	-11.1	-44.4	-35.6	0.33
MIROC-ESM-CHEM						
G4 – RCP4.5	-2.1	9.8	-19.1	-37.4	-27.6	0.55
GEOSCCM						
G4 nhc – RCP4.5	-1.9	21.6	-32.8	-64.5	-42.9	0.49
ULAQ-CCM						
G4 nhc – RCP4.5	-9.7	127	-23.6	-361	-234	3.08
GISS-E2-R						
G3 – RCP4.5	-2.8	4.4	-38.9	-76.8	-72.4	0.99
ULAQ-CCM						
G3 nhc – RCP4.5	-1.9	22.7	-29.5	-60.9	-38.2	0.48
ULAQ-CCM						
G3 nhc – RCP4.5	-2.1	31.7	-7.5	-61.8	-30.1	0.69
GISS-E2-R						

^aValues shown are annually and globally averaged for the whole decade 2040–2049. RF values are calculated as in Table 3.

reduction consequently reduces diabatic heating, resulting in a polar temperature decrease larger than that in the other models above 50 hPa, and of comparable magnitude below 50 hPa, where heterogeneous reactions on PSCs dominate. Significant differences in ozone loss changes due to geoengineering between different models indicate large uncertainties in the model response that depend on various factors (previously highlighted), as differences in climate sensitivity, interactive or prescribed SSTs, QBO treatment, subtropical

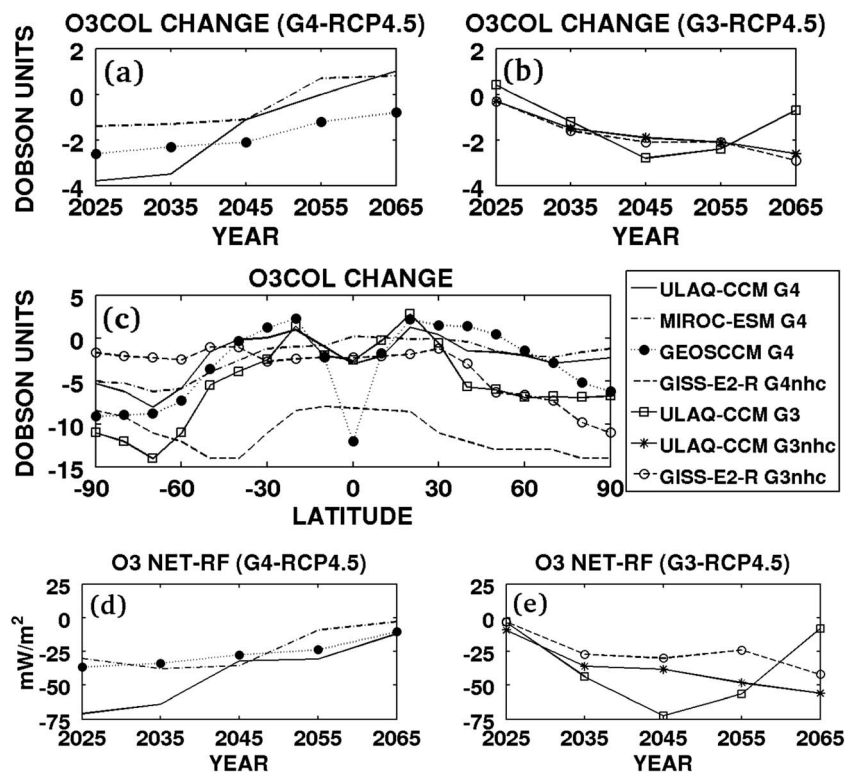


Figure 14. Time series of global O₃ column changes in (a) G4 and (b) G3, with respect to the base case (DU), averaged per decade. (c) Zonally and time-averaged column ozone changes (2040–2049) with respect to RCP4.5. (d, e) As in Figures 14a and 14b, but for net adjusted tropopause RF (mW/m²).

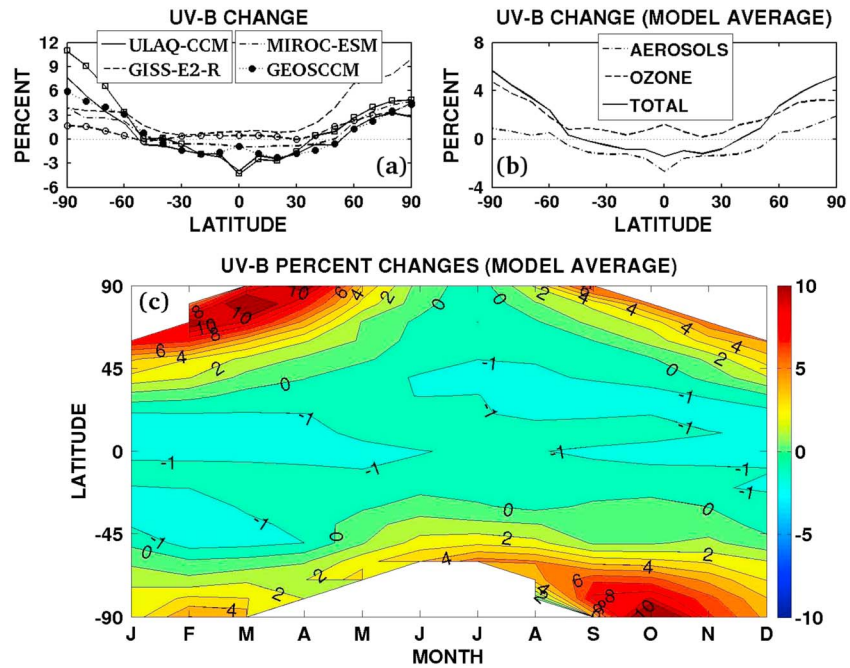


Figure 15. Annually and zonally averaged UV-B percent changes at the surface, due to ozone and aerosol perturbations in G3 and G4, with respect to RCP4.5 (average 2040–2049). (a) Results for the different models, with line styles as specified in the legend (for G4); solid line with open squares and dashed line with open circles refer to G3 simulations of ULAQ-CCM and GISS-E2-R, respectively. (b) Model average of the results, with dashed line for UV-B changes due to ozone perturbations only, dash-dotted line for aerosol perturbations only, solid line for the total. (c) Model average of the zonally averaged values as a function of months (aerosol and ozone perturbations).

horizontal mixing, differences in sulfate aerosol SAD and heterogeneous chemistry, aerosol radiative properties, distribution, and concentration.

4.2. Column Ozone Changes and Ozone Radiative Forcing

Globally, the injection of geoengineering aerosol leads to a reduction of the ozone column in all models for the central decade of experiments G3 and G4 (2040–2049) (see Table 5). Despite the constant stratospheric aerosol loading in G4, the magnitude of the geoengineering aerosol induced ozone depletion decreases in time (Figure 14a) due to the decreasing atmospheric chlorine concentrations. ULAQ-CCM and MIROC-ESM-CHEM even simulate an increase in ozone starting from about 2050, when the ozone increase due to the suppression of the NO_x cycle is no longer balanced by the decrease in total column due to ClO_x and HO_x .

On the other hand, the models simulate an increasing magnitude of ozone depletion in G3. If no heterogeneous chemistry is included in the simulations (ULAQ-CCM nhc and GISS-E2-R nhc), the increasing stratospheric aerosol burden leads to a lower ozone net production during the whole simulated period because of photolysis and temperature changes (Figure 14b). If the heterogeneous chemistry is included (ULAQ-CCM), the depletion of the ozone column is reduced after 2050, because of the increasing importance of NO_x relative to ClO_x . The latitudinal distribution of the ozone column anomaly during 2040–2049 is shown in Figure 14c. The ozone anomaly simulated by GISS-E2-R in G4 is about -15 DU at midlatitudes, 3 times larger than the anomalies simulated by the other models, due to the lack of the heterogeneous NO_x chemistry balancing the photochemical ozone depletion. The difference between GISS-E2-R and the other models decreases at southern high latitudes, where the ozone-depleting chemistry on PSCs particles, which is included in GISS-E2-R, becomes dominant. The other model results for G4 (GEOSCCM, MIROC-ESM-CHEM, and ULAQ-CCM) present a similar latitudinal distribution. GEOSCCM simulates a tropical negative anomaly 3 to 4 times larger than the other models, compatible to the stronger tropical upwelling (Figure 10) and the high tropical isolation in GEOSCCM [Strahan *et al.*, 2011].

The net-adjusted tropopause radiative forcing of ozone (Table 5, Figures 14d and 14e) is calculated off-line with the ULAQ-CCM radiative transfer code. Its time behavior is closely correlated to that of the ozone column changes and ranges from 0 to -0.1 W/m^2 in all models except for the GISS-E2-R G4 case (not shown). In GISS-E2-R

Table 6. Globally Averaged Changes, With Respect to Base Case, of the Following: Aerosol Optical Depth ($\lambda = 0.5 \mu\text{m}$); Stratospheric H_2O Mixing Ratio; O_3 Column; Net Adjusted Tropopause RF of Aerosols, Ozone and Water Vapor; Net Adjusted Total RF of Stratospheric Aerosols and Indirect Stratospheric Effects (O_3 , H_2O); Surface UV-B Percent Change Due to Both Stratospheric Aerosols and Ozone^a

	AOD	H_2O (ppmv)	O_3 Column (DU)	RF-Aerosol (W/m^2)	RF- O_3 (W/m^2)	RF- H_2O (W/m^2)	RF- Net (W/m^2)	UV-B Change (%)
G4 – RCP4.5 ULAQ-CCM	0.068	0.22	–1.1	–1.54	–0.032	0.049	–1.52	–1.04
G4 – RCP4.5 MIROC-ESM-CHEM	0.037	0.02	–1.1	–0.73	–0.036	0.004	–0.76	–0.22
G4 – RCP4.5 GEOSCCM	0.056	0.35	–2.1	–1.27	–0.028	0.077	–1.22	–0.62
G4 – RCP4.5 GISS-E2-R	0.075	–0.36	–9.7	–1.31	–0.234	–0.091	–1.64	2.24
G3 – RCP4.5 ULAQ-CCM	0.060	0.12	–2.8	–1.38	–0.072	0.027	–1.42	–0.33
G3 – RCP4.5 GISS-E2-R	0.010	–0.03	–2.1	–0.17	–0.030	–0.008	–0.21	0.54

^aValues shown are annually averaged for the whole decade 2040–2049.

the O_3 column perturbation is larger (see Table 5 and discussion in section 4.2) and consequently the tropopause net RF increases in magnitude to $-0.23 \text{ W}/\text{m}^2$. These ozone RFs represent a rather small correction (2–10%) of the dominant direct forcing of geoengineering aerosols and are also roughly counterbalanced by the positive radiative forcing associated to the stratospheric H_2O increase (Table 4) produced by the aerosol-driven tropical stratospheric heating rates. Table 5 shows, as expected, that the largest contribution to the O_3 RF comes from the stratospheric temperature adjustment in the longwave range [IPCC/TEAC, 2005].

Through the depletion of the ozone column, the GeoMIP aerosols cause an increase in the global UV-B radiation reaching the surface (Figure 15a). Such an increase is, however, mostly overcompensated (in the tropics) by the scattering of UV-B radiation by the aerosols (Figure 15b). The net effect on the surface UV-B radiation is not meridionally uniform: while the tropics experience a decrease in UV-B radiation reaching the surface, the UV-B over Arctic and Antarctic polar regions increases by about 5% as an annual average, with respect to the base case in 2040–2049, following the ozone column perturbation. These findings are in agreement with *Tilmes et al.* [2012], who found a decrease of 5% erythemal UV in middle and high latitudes and 10% over Antarctica for 2040 if the stratospheric halogen content from very short-lived halogen sources was considered. Figure 15c makes it clear that the largest UV-B relative changes are found during polar springtime months, as a result of the additional polar ozone depletion forced by geoengineering aerosols. It should be noted, however, that although the UV-B polar increases are largely produced by the indirect ozone anomalies caused by geoengineering, they are also, to a lesser extent, a direct consequence of the GeoMIP aerosols, which tend to increase the downward diffused radiation at large solar zenith angles [Tsitas and Yung, 1996]. A well-tested radiative transfer model (TUV) [Madronich and Flocke, 1998] has been used off-line for these UV-B calculations. Regarding potential biological effects, it should be taken into account that the standard atmosphere UV-B irradiance at 80°N April and 80°S October is close to $11 \text{ mW}/\text{m}^2$. This means that the 10% increase associated to the geoengineering aerosol perturbation is negligible in terms of health effects but has to be carefully assessed as environmental impact.

Table 6 summarizes the net radiative perturbations due to aerosols, water vapor, and ozone, as calculated using the off-line ULAQ-CCM radiative transfer code. All models (except GISS-E2-R) predict a net decrease of the globally averaged surface UV-B from -0.22% up to -1.04% : the positive perturbation in GISS-E2-R is a consequence of larger column ozone changes with respect to the other models. The combined indirect RF from water vapor and ozone accounts for -3.7% , -1.1% , and $+4.4\%$ of the RF from aerosols in GEOSCCM, ULAQ-CCM, and MIROC-ESM-CHEM G4 simulations, respectively, and about $+25\%$ from the GISS-E2-R G4 simulation.

5. Conclusions

We have described the ozone changes in simulations of GeoMIP experiments G3 and G4 in an ensemble of models. A summary of model evaluation for past ozone distribution and trends has been presented in this

study: models are in general able to reproduce observed characteristics of the stratosphere (as discussed in detail in WMO and IPCC assessments). In particular, the modeled climatological mean vertical profiles of ozone and the latitudinal distributions at 50 hPa are normally within the interannual standard deviation (1σ) of HALOE mean, as well as the calculated total ozone column in the 1σ range of 20 year TOMS measurements. However, models show shortcomings in the presentation of volcanic and geoengineered aerosols and their chemical and dynamical feedbacks (QBO, temperatures, transport, and interactions with the ocean dynamics). Results of the present study show that ozone changes in the tropics as a result of geoengineering are a complex combination of changes due to perturbations of photolysis rates, enhanced upwelling, and enhanced heterogeneous chemistry. Qualitatively, all models show a net reduction of total ozone in the tropics up to 2050. This is a combination of decreasing ozone due to enhanced upwelling, changes in photolysis rates, and increasing ozone in the middle stratosphere due to the suppression of the ozone depleting NO_x cycle. Consistently, the GISS-E2-R model shows larger reduction of column ozone, due the lack of representation of heterogeneous chemistry on aerosol particles. Further, GEOSCCM simulates smaller changes in ozone than the other models, because it does not include photolysis changes due to the geoengineering aerosol. Consistent throughout all the models is the cooling of the Antarctic vortex, induced by photochemical ozone losses and circulation changes, resulting in enhanced polar stratospheric cloud formation, thus promoting ozone depletion. The net effect is a reduction in polar ozone by over 5% in the majority of model simulations.

The presence of a heterogeneous chemistry parameterization on sulfate aerosols increases the importance of NO_x cycle changes relative to that of ClO_x changes. As ClO_x availability is reduced, depletion of the ozone column also lessens: two models predict an increase of the globally averaged column after year 2050. Total ozone negative changes during 2040–2049 are small (1–2 DU), and the ozone radiative forcing is less than -0.1 W m^{-2} . This negative RF due to ozone changes is about 2 orders of magnitude smaller than the one due to geoengineering aerosols in ULAQ-CCM, MIROC-ESM-CHEM, and GEOSCCM. As such, with the exception of polar regions, which show significant increases in UV-B, models predict small impacts on the stratospheric ozone column, as simulated in the two experiments presented here. The polar springtime perturbation of surface UV-B is consistent for all models between 2040 and 2049 compared to the control simulation, reaching peak values of 12% in both polar regions (as an average over all model simulations) and ranging from 7 to 16% at 80°N March and from 6 to 20% at 80°S October (calculated under all-sky approximation). The reduction of UV-B in high latitudes as a result of geoengineering is dominated by the decrease of column ozone in high latitudes for all models and is in agreement with earlier studies [Tilmes *et al.*, 2012]. The increased downward radiation scattering by the geoengineering aerosols (due to the low sun elevation) also plays a role.

These results are potentially heavily dependent upon the experimental design. ULAQ-CCM is the only model included in this study which can represent aerosol microphysical growth; it shows a substantial increase in sulfate aerosol effective radius, consistent with past studies [Heckendorn *et al.*, 2009; English *et al.*, 2012]. A larger aerosol size reduces the radiative efficiency of the aerosols, requiring much more sulfate aerosol mass to achieve a particular desired radiative forcing [Pierce *et al.*, 2010]. Therefore, the effects on ozone described here may be magnified, depending upon the required mass of SO_2 to meet a climate goal. Moreover, these results are likely specific to continuous tropical injections. Modulating the latitudinal and temporal distribution of geoengineering could have different climate effects [MacMartin *et al.*, 2013].

The ozone response to geoengineering differs among models because of the different assumptions for particle size and parameterization of the different processes. However, ULAQ-CCM, MIROC-ESM-CHEM, and GEOSCCM all show that the dominant ozone changing processes in the tropics are the increased upwelling and the suppression of the NO_x cycle, while at midlatitudes, the suppression of the NO_x cycle and the enhancement of ClO_x – BrO_x cycles dominate. The aerosol radiative impact on O_2 photolysis rates also plays a significant role in the lower stratosphere. The large difference between the results of these three models and those from GISS-E2-R also show that changes in heterogeneous chemistry on sulfate particles contribute the most to changes in global ozone. On the other hand, the relative similarity of the results of all four models in the Antarctic region indicates that here the changes in heterogeneous chemistry on PSCs are very important. The models including heterogeneous chemistry on sulfate particles all agree in showing a progressive reduction of global ozone depletion with decreasing chlorine concentration. After about 2050, the geoengineering aerosol still leads to a suppression of the NO_x cycle, and hence to an increase of ozone, but not to a counterbalancing depletion of ozone due to ClO_x and BrO_x cycles.

The four models contributing to this work have been evaluated here and in several past modeling campaigns showed good skills for ozone prediction and trends, as well as for stratospheric transport and climate-chemistry coupling. However, these models also have several well-documented deficiencies, including, for example, and in some cases, insufficient tropical confinement and incomplete representation of heterogeneous chemical reactions. We conclude that despite the presence of these uncertainties, the presented model results showing the impacts of sulfate geoengineering on ozone have some robust features. Several of these uncertainties could be alleviated with a more strict protocol for participating global models. We also encourage larger model participation for any potential future experiments, which will certainly increase confidence in the results. As said before, however, we have identified some responses to geoengineering common across the models and that, therefore, can be considered robust. (1) The geoengineering aerosol causes global ozone depletion up to about 2050. The magnitude of the global ozone depletion decreases with time due to decreasing chlorine concentrations. (2) The ozone anomaly at midlatitudes is mainly due to enhanced heterogeneous chemistry on aerosol particles. (3) The ozone anomaly in the polar regions is mainly due to enhanced PSCs formation. (4) The ozone anomaly in the tropics results from combination of dynamical, radiative, and chemical perturbations induced by the aerosols (i.e., upwelling, photolysis, and heterogeneous reactions), the first two effects due to absorption and scattering of radiation. (5) The global, latitudinal, and vertical ozone perturbations are rather consistent among the models, producing consistent changes in ozone column, surface UV-B and global tropopause radiative forcing.

The results presented here show only one aspect of geoengineering with stratospheric aerosols when conducted in a certain way. We do not advocate deployment of geoengineering, nor do we suggest ways in which it would be performed. Such decisions should be reserved for legitimate governance structures. Moreover, decisions regarding geoengineering should not be made based solely on physical science studies that need anyhow to rely on improved climate-chemistry modeling results. Social, political, economic, and ethical perspectives also have important roles in informing decisions about geoengineering.

Acknowledgments

We thank all participants of the Geoengineering Model Intercomparison Project and their model development teams, CLIVAR/WCRP Working Group on Coupled Modeling for endorsing GeoMIP, and the scientists managing the Earth System Grid data nodes who have assisted with making GeoMIP output available. We acknowledge the World Climate Research Programme's Working Group on Coupled Modelling, which is responsible for CMIP, and we thank the climate modeling groups for producing and making available their model output. For CMIP the US Department of Energy's Program for Climate Model Diagnosis and Intercomparison provides coordinating support and led development of software infrastructure in partnership with the Global Organization for Earth System Science Portals. Ben Kravitz is supported by the Fund for Innovative Climate and Energy Research (FICER). The Pacific Northwest National Laboratory is operated for the US Department of Energy by Battelle Memorial Institute under contract DE-AC05-76RL01830. Simulations performed by Ben Kravitz and Valentina Aquila were supported by the NASA High-End Computing (HEC) Program through the NASA Center for Climate Simulation (NCCS) at Goddard Space Flight Center. Valentina Aquila is supported by the NASA Modeling, Analysis and Prediction (MAP) program (David Considine, program manager) under the project 08-MAP-80. Shingo Watanabe was supported by the SOUSEI program, MEXT, Japan and the simulations were conducted using the Earth Simulator. Alan Robock was supported by NSF grants AGS-1157525 and CBET-1240507. We acknowledge use of SAGE-II data for stratospheric aerosols.

References

- Aquila, V., L. D. Oman, R. S. Stolarski, P. R. Colarco, and P. A. Newman (2012), Dispersion of the volcanic sulfate cloud from a Mount Pinatubo-like eruption, *J. Geophys. Res.*, *117*, D06216, doi:10.1029/2011JD016968.
- Aquila, V., L. D. Oman, R. S. Stolarski, A. R. Douglass, and P. A. Newman (2013), The response of ozone and nitrogen dioxide to the eruption of Mt. Pinatubo at southern and northern midlatitudes, *J. Atmos. Sci.*, *70*(3), 894–900, doi:10.1175/JAS-D-12-0143.1.
- Bingen, C., D. Fussen, and F. Vanhellemon (2004), A global climatology of stratospheric aerosol size distribution parameters derived from SAGE II data over the period 1984–2000: 1. Methodology and climatological observations, *J. Geophys. Res.*, *109*, D06201, doi:10.1029/2003JD003518.
- Bluth, G. J. S., S. D. Doiron, C. C. Schnetzler, A. J. Krueger, and L. S. Walter (1992), Global tracking of the SO₂ clouds from the June, 1991 Mount Pinatubo eruptions, *Geophys. Res. Lett.*, *19*, 151–154.
- Bodeker, G. E., H. Shiona, and H. Eskes (2005), Indicators of Antarctic ozone depletion, *Atmos. Chem. Phys.*, *5*, 2603–2615.
- Brasseur, G., and C. Granier (1992), Mount Pinatubo aerosols, chlorofluorocarbons, and ozone depletion, *Science*, *257*(5074), 1239–1242.
- Budyko, M. I. (1974), *Climate and Life*, pp. 508, Academic Press, New York.
- Carslaw, K. S., B. P. Luo, and T. Peter (1995), An analytic expression for the composition of aqueous HNO₃–H₂SO₄ stratospheric aerosols including gas phase removal coupled HNO₃, *Geophys. Res. Lett.*, *22*, 1877–1880, doi:10.1029/95GL01668.
- Chin, M., R. B. Rood, S.-J. Lin, and J.-F. Müller (2000), Atmospheric sulfur cycle simulated in the global model GOCART: Model description and global properties, *J. Geophys. Res.*, *105*(D20), 24,671–24,687, doi:10.1029/2000JD900384.
- Chipperfield, M., et al. (2013), SPARC assessment on atmospheric lifetimes, chapter 5: Model estimates of lifetimes, in *SPARC Rep.*, WCRP-15/2013, edited by M. K. W. Ko et al.
- Chou, M.-D., and M. J. Suarez (1999), A solar radiation parameterization for atmospheric studies, *NASA Tech. Rep.*, TM-1999-104606, 50 pp., NASA Goddard Space Flight Cent., Greenbelt, MD.
- Chou, M.-D., M. J. Suarez, X.-Z. Liang, and M. M.-H. Yan (2001), A thermal infrared radiation parameterization for atmospheric studies, *NASA Tech. Rep.*, TM-2001-104606, 68 pp., NASA Goddard Space Flight Cent., Greenbelt, MD.
- Colarco, P., A. Da Silva, M. Chin, and T. Diehl (2010), Online simulations of global aerosol distributions in the NASA GEOS-4 model and comparisons to satellite and ground-based aerosol optical depth, *J. Geophys. Res.*, *115*, D14207, doi:10.1029/2009JD012820.
- Crutzen, P. J. (2006), Albedo enhancement by stratospheric sulfur injections: A contribution to resolve a policy dilemma?, *Clim. Change*, *77*(3–4), 211–220, doi:10.1007/s10584-006-9101-y.
- Dahlback, A., and K. Stamnes (1991), A new spherical model for computing the radiation field available for photolysis and heating at twilight, *Planet. Space Sci.*, *39*, 671–683.
- Deshler, T., D. J. Hofmann, B. J. Johnson, and W. R. Rozier (1992), Balloonborne measurements of the Pinatubo aerosol size distribution and volatility at Laramie, Wyoming during the summer of 1991, *Geophys. Res. Lett.*, *19*(2), 199–202, doi:10.1029/91GL02787.
- Dunkerton, T. J., and D. P. Delisi (1991), Anomalous temperature and zonal wind in the tropical upper stratosphere, 1982/83, *J. Geophys. Res.*, *96*, 22,631–22,641.
- English, J., O. B. Toon, and M. J. Mills (2012), Microphysical simulations of sulfur burdens from stratospheric sulfur geoengineering, *Atmos. Chem. Phys.*, *12*, 4775–4793, doi:10.5194/acp-12-4775-2012.
- Eyring, V., et al. (2006), Assessment of temperature, trace species, and ozone in chemistry-climate model simulation of the recent past, *J. Geophys. Res.*, *111*, D22308, doi:10.1029/2006JD007327.

- Eyring, V., et al. (2013), Long-term ozone changes and associated climate impacts in CMIP5 simulations, *J. Geophys. Res. Atmos.*, *118*, 5029–5060, doi:10.1002/jgrd.50316.
- Fahey, D. W., et al. (1993), *In situ* measurements constraining the role of sulphate aerosols in mid-latitude ozone depletion, *Nature*, *363*, 509–514.
- Fioletov, V. E., G. E. Bodeker, A. J. Miller, R. D. McPeters, and R. Stolarski (2002), Global and zonal total ozone variations estimated from ground-based and satellite measurements: 1964–2000, *J. Geophys. Res.*, *107*(D22), 4647, doi:10.1029/2001JD001350.
- Gent, P. R., et al. (2011), The community climate system model version 4, *J. Clim.*, *24*(19), 4973–4991, doi:10.1175/2011JCLI4083.
- Grant, W. B., et al. (1992), Observations of reduced ozone concentrations in the tropical stratosphere after the eruption of Mt. Pinatubo, *Geophys. Res. Lett.*, *19*, 1109–1112.
- Grooss, J.-U., and J. M. Russell III (2005), Technical note: A stratospheric climatology for O₃, H₂O, CH₄, NO_x, HCl and HF derived from HALOE measurements, *Atmos. Chem. Phys.*, *5*, 2797–2807.
- Hansen, J. E., A. Lacis, R. Ruedy, and M. Sato (1992), Potential climate impact of Mount Pinatubo eruption, *Geophys. Res. Lett.*, *19*, 215–218.
- Hansen, J. E., et al. (2005), Efficacy of climate forcings, *J. Geophys. Res.*, *110*, D18104, doi:10.1029/2005JD005776.
- Hanson, D., and K. Mauersberger (1988), Laboratory studies of the nitric acid trihydrate: Implications for the south polar stratosphere, *Geophys. Res. Lett.*, *15*, 855–858, doi:10.1029/GL015i008p00855.
- Heckendorn, P., D. Weisenstein, S. Fueglistaler, B. P. Luo, E. Rozanov, M. Schraner, L. W. Thomason, and T. Peter (2009), The impact of geoengineering aerosols on stratospheric temperature and ozone, *Environ. Res. Lett.*, *4*, 045,108, doi:10.1088/1748-9326/4/4/045108.
- Hendricks, J., B. Kärcher, and U. Lohmann (2011), Effects of ice nuclei on cirrus clouds in a global climate model, *J. Geophys. Res.*, *116*, D18206, doi:10.1029/2010JD015302.
- IPCC (2013), Climate change 2013: The physical science basis, in *Contribution of Working Group I to the Fifth Assessment Report of the Intergovernmental Panel on Climate Change*, edited by T. F. Stocker et al., 1535 pp., Cambridge Univ. Press, Cambridge, U. K., and New York.
- IPCC/TEAC (2005), Special report on safeguarding the ozone layer and the global climate system: Issues related to hydrofluorocarbons and perfluorocarbons, *Prepared by Working Group I and III of the Intergovernmental Panel on Climate Change, and the Technology and Economic Assessment Panel*, edited by B. Metz et al., 488 pp., Cambridge Univ. Press, Cambridge, U. K., and New York.
- Johnston, P. V., R. L. McKenzie, J. G. Keys, and W. A. Matthews (1992), Observations of depleted stratospheric NO₂ following the Pinatubo volcanic eruption, *Geophys. Res. Lett.*, *19*(2), 211–213.
- Jones, A., et al. (2013), The “termination effect” in experiment G2 of the Geoengineering Model Intercomparison Project (GeoMIP), *J. Geophys. Res. Atmos.*, *118*, 9743–9752, doi:10.1002/jgrd.50762.
- Kärcher, B., and U. Lohmann (2002), A parameterization of cirrus cloud formation: Homogeneous freezing of supercooled aerosols, *J. Geophys. Res.*, *107*(D2), 4010, doi:10.1029/2001JD000470.
- Kinne, S., O. B. Toon, and M. J. Prather (1992), Buffering of stratospheric circulation by changing amounts of tropical ozone: A Pinatubo case study, *Geophys. Res. Lett.*, *19*, 1927–1930.
- Kirchner, I., G. L. Stenchikov, H.-F. Graf, A. Robock, and J. C. Antuna (1999), Climate model simulation of winter warming and summer cooling following the 1991 Mount Pinatubo volcanic eruption, *J. Geophys. Res.*, *104*, 19,039–19,055.
- Koch, D., G. A. Schmidt, and C. V. Field (2006), Sulfur, sea salt, and radionuclide aerosols in GISS ModelE, *J. Geophys. Res.*, *111*, D06206, doi:10.1029/2004JD005550.
- Koike, M., N. B. Jones, W. A. Matthews, P. V. Johnston, R. L. McKenzie, D. Kinnison, and J. Rodriguez (1994), Impact of Pinatubo aerosols on the partitioning between NO₂ and HNO₃, *Geophys. Res. Lett.*, *21*(7), 597, doi:10.1029/94GL00303.
- Koster, R. D., M. J. Suarez, A. Ducharme, M. Stieglitz, and P. Kumar (2000), A catchment-based approach to modeling land surface processes in a general circulation model: 1. Model structure, *J. Geophys. Res.*, *105*(D20), 24,809–24,822, doi:10.1029/2000JD900327.
- Kravitz, B., A. Robock, O. Boucher, H. Schmidt, K. E. Taylor, G. Stenchikov, and M. Schulz (2011a), The Geoengineering Model Intercomparison Project (GeoMIP), *Atmos. Sci. Lett.*, *12*, 162–167, doi:10.1002/asl.316.
- Kravitz, B., A. Robock, O. Boucher, H. Schmidt, and K. E. Taylor (2011b), Specifications for GeoMIP experiments G1 through G4 (Version 1.0). [Available at http://climate.envsci.rutgers.edu/GeoMIP/docs/specificationsG1_G4_v1.0.pdf.]
- Kravitz, B., et al. (2013), Climate model response from the Geoengineering Model Intercomparison Project (GeoMIP), *J. Geophys. Res. Atmos.*, *118*, 8320–8332, doi:10.1002/jgrd.50646.
- Labitzke, K., and M. P. McCormick (1992), Stratospheric temperature increases due to Pinatubo aerosols, *Geophys. Res. Lett.*, *19*, 207–210.
- Lacis, A., J. E. Hansen, and M. Sato (1992), Climate forcing by stratospheric aerosols, *Geophys. Res. Lett.*, *19*, 1607–1610.
- Lamarque, J. F., et al. (2013), The Atmospheric Chemistry and Climate Model Intercomparison Project (ACCMIP): Overview and description of models, simulations and climate diagnostics, *Geosci. Model Dev.*, *6*, 179–206.
- Lambert, A., R. G. Grainger, J. J. Remedios, C. D. Rodgers, M. Corney, and F. W. Taylor (1993), Measurements of the evolution of the Mt. Pinatubo aerosol cloud by ISAM, *Geophys. Res. Lett.*, *20*, 1287–1290.
- Lean, J. (2000), Evolution of the Sun’s spectral irradiance since the Maunder Minimum, *Geophys. Res. Lett.*, *27*, 2425–2428.
- Lin, S.-J. (2004), A “vertically Lagrangian” finite-volume dynamical core for global models, *Mon. Weather Rev.*, *132*, 2293–2307, doi:10.1175/1520-0493(2004)132<2293:AVLFDC>2.0.CO;2.
- Lock, A. P., A. R. Brown, M. R. Bush, G. M. Martin, and R. N. B. Smith (2000), A new boundary layer mixing scheme. Part I: Scheme description and single-column model tests, *Mon. Weather Rev.*, *128*, 3187–3199, doi:10.1175/1520-0493(2000)128<3187:ANBLMS>2.0.CO;2.
- Long, C. S., and L. L. Stowe (1994), Using the NOAA/AVHRR to study stratospheric aerosol optical thickness following the Mt. Pinatubo eruption, *Geophys. Res. Lett.*, *21*, 2215–2218.
- Louis, J., M. Tiedtke, and J. Geleyn (1982), A short history of the PBL parameterization at ECMWF, paper presented at ECMWF Workshop on Planetary Boundary Layer Parameterization, Eur. Cent. for Medium-Range Weather Forecasts, Reading, U. K.
- MacMartin, D. G., D. W. Keith, B. Kravitz, and K. Caldeira (2013), Managing trade-offs in geoengineering through optimal choice of non-uniform radiative forcing, *Nat. Clim. Change*, *3*, 365–368, doi:10.1038/nclimate1722.
- Madronich, S., and S. Flocke (1998), The role of solar radiation in atmospheric chemistry, in *Handbook of Environmental Chemistry*, edited by P. Boule, pp. 1–26, Springer, Heidelberg.
- McCormick, M. P., and R. E. Veiga (1992), SAGE II measurements of early Pinatubo aerosols, *Geophys. Res. Lett.*, *19*, 155–158.
- McCormick, M. P., L. W. Thomason, and C. R. Trepte (1995), Atmospheric effects of the Mt. Pinatubo eruption, *Nature*, *373*, 399–404.
- Meinshausen, M., et al. (2011), The RCP greenhouse gas concentrations and their extensions from 1765 to 2300, *Clim. Change*, *109*, 213–241, doi:10.1007/s10584-011-0156-z.
- Miller, A. J., et al. (2002), A cohesive total ozone data set from the SBUV(2) satellite system, *J. Geophys. Res.*, *107*(D23), 4701, doi:10.1029/2001JD000853.
- Minschwaner, K., R. J. Salawitch, and M. B. McElroy (1993), Absorption of Solar Radiation by O₂: Implications for O₃ and lifetimes of N₂O, CFCl₃, and CF₂Cl₂, *J. Geophys. Res.*, *98*, 10,543–10,561, doi:10.1029/93JD00223.

- Molod, A., L. Takacs, M. Suarez, J. Bacmeister, I.-S. Song, and A. Eichmann (2012), The GEOS-5 atmospheric general circulation model: Mean climate and development from MERRA to Fortuna, *Tech. Rep. Series on Global Modeling and Data Assimilation, NASA TM-2012-104606*, vol. 28.
- Moorthi, S., and M. J. Suarez (1992), Relaxed Arakawa-Schubert. A parameterization of moist convection for general circulation models, *Mon. Weather Rev.*, *120*, 978–1002, doi:10.1175/1520-0493(1992)120<0978:RASAP0>2.0.CO;2.
- Morgenstern, O., et al. (2010), A review of CCMVal-2 models and simulations, *J. Geophys. Res.*, *115*, D00M02, doi:10.1029/2009JD013728.
- Niemeier, U., H. Schmidt, and C. Timmreck (2011), The dependency of geoengineered sulfate aerosol on the emission strategy, *Atmos. Sci. Lett. Spec. Issue Geoeng.*, *12*(2), 189–194.
- Pawson, S., R. S. Stolarski, A. R. Douglass, P. A. Newman, J. E. Nielsen, S. M. Frith, and M. L. Gupta (2008), Goddard Earth Observing System chemistry-climate model simulations of stratospheric ozone-temperature coupling between 1950 and 2005, *J. Geophys. Res.*, *113*, D121103, doi:10.1029/2007JD009511.
- Petters, M. D., and S. M. Kreidenweis (2007), A single parameter representation of hygroscopic growth and cloud condensation nucleus activity, *Atmos. Chem. Phys.*, *7*(8), 1961–1971.
- Pierce, J. R., D. K. Weisenstein, P. Heckendorn, T. Peter, and D. W. Keith (2010), Efficient formation of stratospheric aerosol for climate engineering by emission of condensable vapor from aircraft, *Geophys. Res. Lett.*, *37*, L18805, doi:10.1029/2010GL043975.
- Pitari, G. (1993), A numerical study of the possible perturbation of stratospheric dynamics due to Pinatubo aerosols: Implications for tracer transport, *J. Atmos. Sci.*, *50*, 2443–2461.
- Pitari, G., and E. Mancini (2002), Short-term climatic impact of the 1991 volcanic eruption of Mt. Pinatubo and effects on atmospheric tracers, *Nat. Hazard. Earth Syst. Sci.*, *2*, 91–108, doi:10.5194/nhess-2-91-2002.
- Pitari, G., and V. Rizi (1993), An estimate of the chemical and radiative perturbation of stratospheric ozone following the eruption of Mt. Pinatubo, *J. Atmos. Sci.*, *50*, 3260–3276.
- Pitari, G., E. Mancini, V. Rizi, and D. T. Shindell (2002), Impact of future climate and emission changes on stratospheric aerosols and ozone, *J. Atmos. Sci.*, *59*, 414–440.
- Prather, M. J. (1992), Catastrophic loss of stratospheric ozone in dense volcanic clouds, *J. Geophys. Res.*, *97*, 10,187–10,191.
- Randles, C. A., et al. (2013), Intercomparison of shortwave radiative transfer schemes in global aerosol modeling: Results from the AeroCom Radiative Transfer Code Experiment, *Atmos. Chem. Phys.*, *13*, 2347–2379, doi:10.5194/acp-13-2347-2013.
- Rayner, N. A., D. E. Parker, E. B. Horton, C. K. Folland, L. V. Alexander, D. P. Rowell, E. C. Kent, and A. Kaplan (2003), Global analyses of sea surface temperature, sea ice, and night marine air temperature since the late nineteenth century, *J. Geophys. Res.*, *108*(D14), 4407, doi:10.1029/2002JD002670.
- Read, W. G., L. Froidevaux, and J. W. Waters (1993), Microwave limb sounder measurements of stratospheric SO₂ from the Mt. Pinatubo volcano, *Geophys. Res. Lett.*, *20*, 1299–1302.
- Rienecker, M. M., et al. (2011), MERRA: NASA's Modern-Era Retrospective Analysis for Research and Applications, *J. Clim.*, *24*(14), 3624–3648, doi:10.1175/JCLI-D-11-00015.1.
- Robock, A. (2000), Volcanic eruptions and climate, *Rev. Geophys.*, *38*, 191–219, doi:10.1029/1998RG000054.
- Robock, A., L. Oman, and G. L. Stenchikov (2008), Regional climate responses to geoengineering with tropical and Arctic SO₂ injections, *J. Geophys. Res.*, *113*, D16101, doi:10.1029/2008JD010050.
- Russell, G. L., J. R. Miller, and D. Rind (1995), A coupled atmosphere-ocean model for transient climate change, *Atmos. Ocean*, *33*, 683–730.
- Sander, S. P., et al. (2011), Chemical Kinetics and Photochemical Data for Use in Atmospheric Studies, Evaluation Number 17, JPL Publ. # 10–6, NASA-JPL-Caltech, Pasadena, CA, USA.
- Sato, M., J. E. Hansen, M. P. McCormick, and J. B. Pollack (1993), Stratospheric aerosol optical depth, 1850–1990, *J. Geophys. Res.*, *98*, 22,987–22,994, doi:10.1029/93JD02553.
- Schmidt, G. A., et al. (2006), Present-day atmospheric simulations using GISS ModelE: Comparison to in situ, satellite and reanalysis data, *J. Clim.*, *19*, 153–192, doi:10.1175/JCLI3612.1.
- Schoeberl, M. R., P. K. Bhartia, and E. Hilsenrath (1993), Tropical ozone loss following the eruption of Mt. Pinatubo, *Geophys. Res. Lett.*, *20*, 29–32.
- Shepherd, J., et al. (2009), *Geoengineering the Climate: Science, Governance, and Uncertainty*, Royal Society Policy document 10/09, pp. 82, Royal Society, London, U. K.
- Shindell, D. T., G. Faluvegi, N. Unger, E. Aguilar, G. A. Schmidt, D. M. Koch, S. E. Bauer, and R. L. Miller (2006), Simulations of preindustrial, present-day, and 2100 conditions in the NASA GISS composition and climate model G-PUCINI, *Atmos. Chem. Phys.*, *6*, 4427–4459, doi:10.5194/acp-6-4427-2006.
- Soden, B. J., R. T. Wetherald, G. L. Stenchikov, and A. Robock (2002), Global cooling after the eruption of Mount Pinatubo: A test of climate feedback by water vapor, *Science*, *296*(5568), 727–730, doi:10.1126/science.296.5568.727.
- Solomon, S. (1999), Stratospheric ozone depletion: A review of concepts and history, *Rev. Geophys.*, *37*, 275–316, doi:10.1029/1999RG900008.
- SPARC-CCMVal (2010), SPARC Report on the evaluation of chemistry-climate models, in *SPARC Report, WCRP-132, WMO/TD-No. 1526*, edited by V. Eyring, T. G. Shepherd, and D. W. Waugh.
- Stenchikov, G. L., I. Kirchner, A. Robock, H.-F. Graf, J. C. Antuna, R. Grainger, A. Lambert, and L. Thomason (1998), Radiative forcing from the 1991 Mt. Pinatubo volcanic eruption, *J. Geophys. Res.*, *103*, 13,837–13,858.
- Stieglitz, M., A. Ducharme, R. Koster, and M. Suarez (2001), The impact of detailed snow physics on the simulation of snow cover and sub-surface thermodynamics at continental scales, *J. Hydrometeorol.*, *2*(3), 228–242, doi:10.1175/1525-7541(2001)002<0228:TODSP>2.0.CO;2.
- Stolarski, R. S., and S. M. Frith (2006), Search for evidence of trend slow-down in the long-term TOMS/SBUV total ozone data record: The importance of instrument drift uncertainty, *Atmos. Chem. Phys.*, *6*, 4057–4065.
- Strahan, S. E., et al. (2011), Using transport diagnostics to understand chemistry climate model ozone simulations, *J. Geophys. Res.*, *116*, D17302, doi:10.1029/2010JD015360.
- Tang, I. N. (1996), Chemical and size effects of hygroscopic aerosols on light scattering coefficients, *J. Geophys. Res.*, *101*(D14), 19,245–19,250.
- Taylor, K. E., R. J. Stouffer, and G. A. Meehl (2012), An overview of CMIP5 and the experiment design, *Bull. Am. Meteorol. Soc.*, *93*, 485–498, doi:10.1175/BAMS-D-11-00094.1.
- Telford, P., P. Braesicke, O. Morgenstern, and J. Pyle (2009), Reassessment of causes of ozone column variability following the eruption of Mount Pinatubo using a nudged CCM, *Atmos. Chem. Phys.*, *9*, 4251–4260, doi:10.5194/acp-9-4251-2009.
- Thomason, L. W., L. R. Poole, and T. Deshler (1997), A global climatology of stratospheric aerosol surface area density deduced from stratospheric aerosol and gas experiment II measurement: 1984–1994, *J. Geophys. Res.*, *102*(D7), 8967–8976, doi:10.1029/96JD02962.
- Tie, X., and G. Brasseur (1995), The response of stratospheric ozone to volcanic eruptions: Sensitivity to atmospheric chlorine loading, *Geophys. Res. Lett.*, *22*(22), 3035–3038, doi:10.1029/95GL03057.

- Tilmes, S., R. Müller, and R. Salawitch (2008), The sensitivity of polar ozone depletion to proposed geoengineering schemes, *Science*, 320(5880), 1201–1204, doi:10.1126/science.1153966.
- Tilmes, S., R. R. Garcia, D. E. Kinnison, A. Gettelman, and P. J. Rasch (2009), Impact of geoengineered aerosols on the troposphere and stratosphere, *J. Geophys. Res.*, 114, D12305, doi:10.1029/2008JD011420.
- Tilmes, S., D. E. Kinnison, R. R. Garcia, R. Salawitch, T. Canty, J. Lee-Taylor, S. Madronich, and K. Chance (2012), Impact of very short-lived halogens on stratospheric ozone abundance and UV radiation in a geo-engineered atmosphere, *Atmos. Chem. Phys.*, 12, 10,945–10,955, doi:10.5194/acp-12-10945-2012.
- Toon, O. B., C. P. McKay, T. P. Ackerman, and K. Santhanam (1989), Rapid calculation of radiative heating rates and photodissociation rates in inhomogeneous multiple scattering atmospheres, *J. Geophys. Res.*, 94, 16,287–16,301, doi:10.1029/JD094iD13p16287.
- Tsitas, S. R., and Y. L. Yung (1996), The effect of volcanic aerosols on ultraviolet radiation in Antarctica, *Geophys. Res. Lett.*, 23, 157–160.
- Watanabe, S., et al. (2011a), MIROC-ESM: Model description and basic results of CMIP5-20c3m experiments, *Geosci. Model Dev. Discuss.*, 4, 1063–1128, doi:10.5194/gmd-4-1063-2011.
- Watanabe, S., K. Sudo, T. Nagashima, T. Takemura, H. Kawase, and T. Nozawa (2011b), Future projections of surface UV-B in a changing climate, *J. Geophys. Res.*, 116, D16118, doi:10.1029/2011JD015749.
- Weisenstein, D., S. Bekki, G. Pitari, C. Timmreck, and M. Mills (2006), WCRP/SPARC scientific assessment of stratospheric aerosol properties; Chapter 6: Modeling of stratospheric aerosols, *SPARC Rep. 4, WCRP-124, WMO/TD-1295*, edited by L. Thomason and T. Peter.
- WMO/UNEP (2011), Scientific assessment of ozone depletion: 2010, *Global Ozone Res. Monit. Proj. Rep. 52*, 516 pp., Geneva, Switzerland.
- Young, R. E., H. Houben, and O. B. Toon (1994), Radiatively forced dispersion of the Mt. Pinatubo volcanic cloud and induced temperature perturbations in the stratosphere during the first few months following the eruption, *Geophys. Res. Lett.*, 21, 369–372.
- Young, P. J., et al. (2013), Pre-industrial to end 21st century projections of tropospheric ozone from the Atmospheric Chemistry and Climate Model Intercomparison Project (ACCMIP), *Atmos. Chem. Phys.*, 13, 2063–2090.